6 Radiative transfer and optical imaging in biological media by low-order transport approximations: the simplified spherical harmonics (SP_N) approach

Jorge Bouza Domínguez and Yves Bérubé-Lauzière

6.1 Introduction

Radiative transfer theory (RTT) is a valuable theoretical framework for describing the propagation of optical radiation in turbid media (Ishimaru, 1978; Wang and Wu, 2007). RTT has succeeded in fields such as astronomy and astrophysics (Chandrasekhar, 1960), remote sensing of the earth surface and atmosphere (Melnikova et al., 2012), heat transfer (Howell et al., 2010; Modest, 2003; Atalay, 2006), and, particularly, in biomedical optics (Wang and Wu, 2007; Hielscher et al., 2011; Klose, 2010a). The fundamental equation in RTT is the radiative transfer equation (RTE) (Wang and Wu, 2007). The RTE is the most accurate model for describing light propagation in biological tissue, with no approximation regarding the angular, spatial or temporal dependences (Hielscher et al., 2011). The RTE is an integro-differential equation that depends on a set of optical parameters (index of refraction, absorption, scattering and scattering function) that describe the medium (Ishimaru, 1978). The validity limits of the RTE rest on the model conceived to describe light propagation, and should be established for each physical situation (Martí López et al., 2003). Analytical solutions of the RTE are only known for simple geometries (Ishimaru, 1978; Liemert and Kienle, 2011b). Thus, numerical techniques are used in practical situations where complex geometries and/or heterogeneous optical property distributions need to be considered (Tarvainen, 2006). Solving the RTE for biological media carries a considerable numerical burden (Tarvainen, 2006; Klose and Larsen, 2006). In imaging applications, the RTE needs to be solved anew at each iteration step of an optimization algorithm in order to determine optimal optical parameters (Dehghani et al., 2009b; Arridge and Schotland, 2009). This is an implicit limitation of RTE-based image reconstruction algorithms in pre-clinical and clinical imaging and therapeutics, where the diagnosis time matters.

To reduce computation time, the diffusion equation (DE) is frequently used instead of the RTE (Wang and Wu, 2007; Dehghani et al., 2009b). The DE is derived from the RTE using the diffusion approximation which assumes that the field appearing in the RTE is almost isotropic at each point (Ishimaru, 1978; Wang and Wu, 2007). Unfortunately, there are several practical situations where the DE fails, as in the vicinity of sources (Martí López et al., 2004) and in the case of small geometries, low scattering, or high absorption (Hielscher et al., 1998; Chen et al.,

A.A. Kokhanovsky (ed.), *Light Scattering Reviews 8: Radiative transfer and light scattering*,
Springer Praxis Books, DOI 10.1007/978-3-642-32106-1_6,

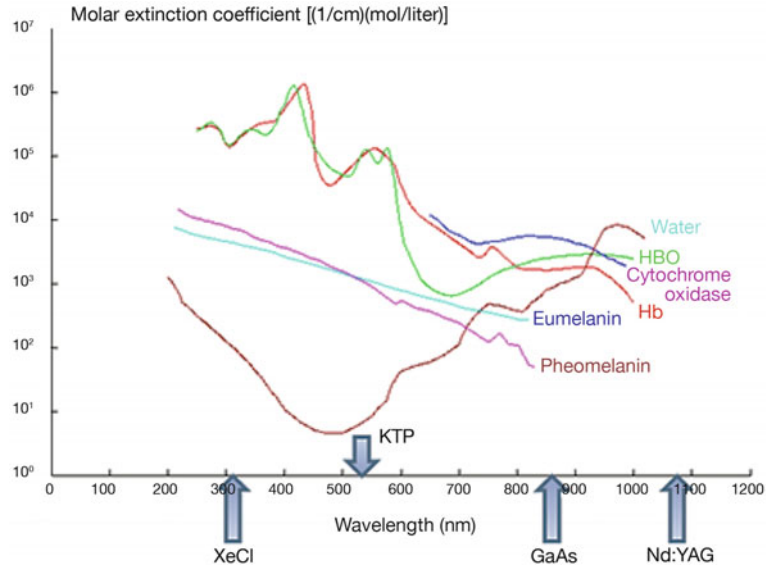

Fig. 6.1. Molar extinction coefficient (absorption/concentration) of several chromophores. Arrows at the bottom indicate the emission wavelength of common lasers.

2001). For example, in the so-called therapeutic window (600 to 1000 nm), vascularized tissues present high absorption because of chromophore absorption spectra, see Fig. 6.1 for the molar extinction coefficient values of common chromophores.

In such circumstances, the radiative field cannot be accurately described by the DE. Then, DE-based radiation dose calculations will yield wrong estimates and spatial resolution and quantitativeness of retrieved optical coefficients maps can be seriously affected. To overcome the drawbacks of the DE and avoid the RTE's computational burden, low-order transport models with simplified angular dependences were recently brought to biomedical optics (Klose and Larsen, 2006; Chu et al., 2009; Bouza Domínguez and Bérubé-Lauzière, 2010; Bouza Domínguez and Bérubé-Lauzière, 2011a). Some of these models are derived from the RTE using the simplified spherical harmonics approximation (SP_N) (Klose and Larsen, 2006). SP_N models have been developed for steady-state – or continuous-wave (CW) (Klose and Larsen, 2006), frequency-domain (FD) (Chu et al., 2009) and time-domain (TD) problems (Bouza Domínguez and Bérubé-Lauzière, 2010; Bouza Domínguez and Bérubé-Lauzière, 2011a), opening new possibilities in treatment and imaging applications of biomedical optics.

We herein review the use of SP_N models in describing radiative transfer in biological media. We also survey the outcomes of using SP_N models in optical imaging. With this, we hope to motivate further developments and applications of SP_N models in therapeutics and optical imaging of biological media.

6.2 Light transport in biological media

In tissue optics, RTT describes the emission, propagation, scattering and absorption of radiation. It provides a macroscopic view of the propagation of light (Ishimaru, 1978). In RTT, only the flow of energy through the medium is considered. Interference and diffraction effects are neglected and magnitudes such as the radiance bear the physical meaning. Through the use of the Stokes vector, polarization can, however, be accounted for in RTT. Additionally, concepts such as ray, ray congruence and ray divergence can be extrapolated from geometrical optics and employed to elaborate a mathematical model of light propagation (Martí López et al., 2003). Applying the law of the conservation of energy in a differential volume element, it is possible to derive an expression for the radiance variation in terms of the optical properties of the medium, leading to the RTE. Corresponding boundary conditions for the radiance can be obtained as well.

In the next section, we write down the expressions for the RTE and its boundary conditions. We introduce the reduced incident and the diffused radiance its corresponding components and review two well-known approximations: the spherical harmonics approximation leading to the so-called P_N equations, and the diffusion approximation (DA) leading to the DE.

6.2.1 The radiative transfer equation

The standard way of deriving the RTE[1] leads to the following expression (Wang and Wu, 2007)

$$\begin{aligned}\frac{\eta}{c}\frac{\partial}{\partial t}L(\mathbf{r},\widehat{\mathbf{s}},t)+\widehat{\mathbf{s}}\cdot\nabla L(\mathbf{r},\widehat{\mathbf{s}},t)\\ =-\left[\mu_{\mathrm{a}}(\mathbf{r})+\mu_{\mathrm{s}}(\mathbf{r})\right]L\left(\mathbf{r},\widehat{\mathbf{s}},t\right)+\mu_{\mathrm{s}}(\mathbf{r})\int_{4\pi}p(\mathbf{r},\widehat{\mathbf{s}},\widehat{\mathbf{s}}')L(\mathbf{r},\widehat{\mathbf{s}}',t)\,\mathrm{d}\Omega'+q\left(\mathbf{r},\widehat{\mathbf{s}},t\right),\end{aligned} \tag{6.1}$$

where $L(\mathbf{r},\widehat{\mathbf{s}},t)$ is the radiance at point $\mathbf{r}$ in the direction specified by the unit vector $\widehat{\mathbf{s}}$, η is the refractive index, c is the speed of light in vacuum, $\mu_{\mathrm{a}}(\mathbf{r})$ and $\mu_{\mathrm{s}}(\mathbf{r})$ are respectively the absorption and scattering coefficients, $p(\mathbf{r},\widehat{\mathbf{s}},\widehat{\mathbf{s}}')$ is the normalized scattering function (also customarily called the 'phase function') which represents the probability of a photon being scattered in direction $\widehat{\mathbf{s}}$ when coming from direction $\widehat{\mathbf{s}}'$, $\mathrm{d}\Omega'$ is a differential element of solid angle, $q(\mathbf{r},\widehat{\mathbf{s}},t)$ is a source distribution per unit volume and ∇ denotes the gradient operator with respect to the $\mathbf{r}$ coordinates.

Frequently, the radiance is decomposed into collimated and diffuse components and Eq. (6.1) is posed in terms of the latter (Ishimaru, 1978). This approach is quite useful when applying low-order transport approximations since the angular dependence of the diffuse radiance is less pronounced than the total radiance. Hence, low-order transport approximations better reproduce (with the addition of the col-

[1] In the standard derivation of the RTE, the refractive index is a piecewise constant function not a continuous function. Besides, ray divergence effects are neglected in the discussion here (Martí López et al., 2003).

limated component) the radiative field than full RTE-based low-order transport approximations. In addition, we point out the fact that measurements in diffuse optical tomography (DOT) are done in terms of the diffused component only.

The solution of Eq. (6.1) requires the specification of initial and boundary conditions. For a smooth tissue–air interface ∂V and in the presence of specular Fresnel reflection, the vacuum boundary condition is substituted by the partly-reflecting boundary condition (Case and Zweifel, 1967; Duderstadt and Martin, 1979; Ishimaru, 1978)

$$L(\mathbf{r}', \widehat{\mathbf{s}}, t) = B_T(\mathbf{r}', \widehat{\mathbf{s}}, t) + R_F(\widehat{\mathbf{n}} \cdot \widehat{\mathbf{s}}')L(\mathbf{r}', \widehat{\mathbf{s}}', t)\,, \quad \mathbf{r}' \in \partial V,\ \widehat{\mathbf{s}} \cdot \widehat{\mathbf{n}} < 0\,, \tag{6.2}$$

where R_F is the angle dependent Fresnel coefficient (Born and Wolf, 2003), $B_T(\mathbf{r}, \widehat{\mathbf{s}}, t)$ is the radiance of the exterior source transmitted inside the medium, $\widehat{\mathbf{n}}$ is the outer normal to the surface ∂V and $\widehat{\mathbf{s}}' = \widehat{\mathbf{s}} - 2\big(\widehat{\mathbf{n}} \cdot \widehat{\mathbf{s}}\big)\widehat{\mathbf{n}}$. Here, $\widehat{\mathbf{s}}'$ is a vector that points outward and is the specular reflection of vector $\widehat{\mathbf{s}}$. For a smooth tissue–tissue interface, the flux balance can be expressed as Marshak conditions (Marshak, 1947; Davidson and Sykes, 1957; Faris, 2002)

$$\begin{aligned}
\int_{\widehat{\mathbf{s}}\cdot\widehat{\mathbf{n}}>0} L_1(\mathbf{r}, \widehat{\mathbf{s}}, t)\,(\widehat{\mathbf{s}} \cdot \widehat{\mathbf{n}})\,\mathrm{d}\Omega &= \int_{\widehat{\mathbf{s}}\cdot\widehat{\mathbf{n}}<0} R_{F,1} L_1(\mathbf{r}, \widehat{\mathbf{s}}, t)\,(-\widehat{\mathbf{s}} \cdot \widehat{\mathbf{n}})\,\mathrm{d}\Omega \\
&\quad + \int_{\widehat{\mathbf{s}}\cdot\widehat{\mathbf{n}}>0} \left[1 - R_{F,2}\right] L_2(\mathbf{r}, \widehat{\mathbf{s}}, t)\,(\widehat{\mathbf{s}} \cdot \widehat{\mathbf{n}})\,\mathrm{d}\Omega \\
\int_{\widehat{\mathbf{s}}\cdot\widehat{\mathbf{n}}<0} L_2(\mathbf{r}, \widehat{\mathbf{s}}, t)\,(-\widehat{\mathbf{s}} \cdot \widehat{\mathbf{n}})\,\mathrm{d}\Omega &= \int_{\widehat{\mathbf{s}}\cdot\widehat{\mathbf{n}}>0} R_{F,2} L_2(\mathbf{r}, \widehat{\mathbf{s}}, t)\,(\widehat{\mathbf{s}} \cdot \widehat{\mathbf{n}})\,\mathrm{d}\Omega \\
&\quad + \int_{\widehat{\mathbf{s}}\cdot\widehat{\mathbf{n}}<0} \left[1 - R_{F,1}\right] L_1(\mathbf{r}, \widehat{\mathbf{s}}, t)\,(-\widehat{\mathbf{s}} \cdot \widehat{\mathbf{n}})\,\mathrm{d}\Omega
\end{aligned} \tag{6.3}$$

where $L_i(\mathbf{r}, \widehat{\mathbf{s}}, t)$ denotes the radiance in medium $i = 1, 2$ and $R_{\mathrm{F},i}$ is the angle dependent Fresnel reflection coefficient for medium i.

6.2.2 Spherical harmonics expansion and the $\mathbf{P}_N$ approximation

In the spherical harmonics expansion, the transport equation is reduced to a system of coupled partial differential equations (PDEs) with no angular-dependence (Case and Zweifel, 1967; Davidson and Sykes, 1957). The angular dependent functions appearing in Eq. (6.1), such as the radiance $L(\mathbf{r}, \widehat{\mathbf{s}}, t)$ and the source distribution $q\big(\mathbf{r}, \widehat{\mathbf{s}}, t\big)$, are expanded along spherical harmonics $Y_{l,m}(\widehat{\mathbf{s}}) \equiv Y_{l,m}(\theta, \phi)$ (θ and ϕ being respectively the polar and the azimuthal angles of spherical coordinates) as

$$L(\mathbf{r}, \widehat{\mathbf{s}}, t) = \sum_{l=0}^{\infty} \sum_{m=-l}^{l} \left(\frac{2l+1}{4\pi}\right)^{\frac{1}{2}} \psi_{l,m}(\mathbf{r}, t) Y_{l,m}(\widehat{\mathbf{s}})\,, \tag{6.4}$$

$$q(\mathbf{r}, \widehat{\mathbf{s}}, t) = \sum_{l=0}^{\infty} \sum_{m=-l}^{l} \left(\frac{2l+1}{4\pi}\right)^{\frac{1}{2}} q_{l,m}(\mathbf{r}, t) Y_{l,m}(\widehat{\mathbf{s}})\,, \tag{6.5}$$

where, following (Case-Zweifel, 1967), the normalization factor $\left[(2l+1)/4\pi\right]^{\frac{1}{2}}$ is introduced for the convenience that it results in simpler final expressions. Properties of the spherical harmonics can be found in (Abramowitz and Stegun, 1965).

For the scattering function $p(\mathbf{r},\widehat{\mathbf{s}},\widehat{\mathbf{s}}')$, the reasonable assumption is made that it only depends on the angular change between the incident and the scattered directions of a photon, i.e. $p(\mathbf{r},\widehat{\mathbf{s}},\widehat{\mathbf{s}}') = p(\mathbf{r},\widehat{\mathbf{s}}\cdot\widehat{\mathbf{s}}')$. In this case, the phase function can be expanded along Legendre polynomials as

$$p(\mathbf{r},\widehat{\mathbf{s}}\cdot\widehat{\mathbf{s}}') = \sum_{l=0}^{\infty}\sum_{m=-l}^{l}\left(\frac{2l+1}{4\pi}\right)p_l(\mathbf{r},t)P_l(\widehat{\mathbf{s}}\cdot\widehat{\mathbf{s}}')\,. \tag{6.6}$$

Making use of the addition theorem for spherical harmonics, this can be rewritten as

$$p(\mathbf{r},\widehat{\mathbf{s}}\cdot\widehat{\mathbf{s}}') = \sum_{l=0}^{\infty}\sum_{m=-l}^{l}p_l(\mathbf{r})Y_{l,m}(\widehat{\mathbf{s}})Y_{l,m}(\widehat{\mathbf{s}}')\,. \tag{6.7}$$

Inserting Eqs. (6.4), (6.5) and (6.7) into Eq. (6.1) and after some algebra (see recurrence relations for $Y_{l,m}(\widehat{\mathbf{s}})$ in (Abramowitz and Stegun, 1965), an infinite set of coupled PDEs is obtained

$$\begin{aligned}
&\left(\frac{\eta}{c}\frac{\partial}{\partial t}+\mu_{tr}(\mathbf{r})\right)\psi_{l,m}(\mathbf{r},t)\\
&\quad+\frac{1}{2l+1}\left(\frac{\partial}{\partial z}\Big[(l+1-m)^{\frac{1}{2}}(l+1+m)^{\frac{1}{2}}\psi_{l+1,m}(\mathbf{r},t)+(l-m)^{\frac{1}{2}}(l+m)^{\frac{1}{2}}\psi_{l-1,m}(\mathbf{r},t)\Big]\right.\\
&\quad-\frac{1}{2}\left(\frac{\partial}{\partial x}-i\frac{\partial}{\partial y}\right)\Big[(l+m)^{\frac{1}{2}}(l+m-1)^{\frac{1}{2}}\psi_{l-1,m-1}(\mathbf{r},t)\\
&\qquad\qquad-(l-m+2)^{\frac{1}{2}}(l-m+1)^{\frac{1}{2}}\psi_{l+1,m-1}(\mathbf{r},t)\Big]\\
&\quad-\frac{1}{2}\left(\frac{\partial}{\partial x}+i\frac{\partial}{\partial y}\right)\Big[-(l-m)^{\frac{1}{2}}(l-m-1)^{\frac{1}{2}}\psi_{l-1,m+1}(\mathbf{r},t)\\
&\qquad\qquad+(l+m+1)^{\frac{1}{2}}(l+m+2)^{\frac{1}{2}}\psi_{l+1,m+1}(\mathbf{r},t)\Big]\Big)\\
&=\mu_s(\mathbf{r})p_l\psi_{l,m}(\mathbf{r},t)+q_{l,m}(\mathbf{r},t)\,,
\end{aligned} \tag{6.8}$$

where $\mu_{tr}(\mathbf{r})=\mu_{\mathrm{a}}(\mathbf{r})+\mu_{\mathrm{s}}(\mathbf{r})$ is the transport coefficient and $i=\sqrt{-1}$. Truncating the series in Eqs. (6.4)–(6.7) at $l=N$ (this is the so-called P_N *approximation*), a system of $(N+1)^2$ coupled first-order PDEs is obtained. These are known as the P_N equations, which have been used as the forward model for imaging the scattering and absorption properties of biological media (Wright et al., 2007). Using the finite element method (FEM) for discretizing the forward model, initial results show an improvement over reconstructions based on the diffusion equation (Wright et al., 2007).

6.2.3 P_1 and the diffusion approximation

Truncating the expansions in Eqs. (6.4)–(6.7) at $l=N=1$ (P_1 approximation), leads to four equations that can be grouped in vector form as (Wang and Wu, 2007)

$$\frac{\eta}{c}\frac{\partial\psi_0(\mathbf{r},t)}{\partial t} + \nabla\cdot\mathbf{J}(\mathbf{r},t) + \mu_a(\mathbf{r})\psi_0(\mathbf{r},t) = \varepsilon_0(\mathbf{r},t)\,, \tag{6.9}$$

$$\frac{\eta}{c}\frac{\partial\mathbf{J}(\mathbf{r},t)}{\partial t} + \frac{1}{3}\nabla\psi_0(\mathbf{r},t) + \left[\mu_a(\mathbf{r}) + \mu'_{\mathrm{s}}(\mathbf{r})\right]\mathbf{J}(\mathbf{r},t) = \boldsymbol{\varepsilon}_1(\mathbf{r},t)\,, \tag{6.10}$$

where $\mu'_{\mathrm{s}} = \mu_{\mathrm{s}}(1-g)$ is the so-called reduced scattering coefficient and g is known as the anisotropy coefficient (Ishimaru, 1978; Wang and Wu, 2007), $\psi_0(\mathbf{r},t)$ and $\mathbf{J}(\mathbf{r},t)$ are the fluence rate and the radiant current density vector, respectively, with $\mathbf{J}$ given by

$$\mathbf{J}(\mathbf{r},t) = \int_{4\pi} L(\mathbf{r},\hat{\mathbf{s}},t)\,\hat{\mathbf{s}}\;\mathrm{d}\Omega = \sqrt{\frac{2\pi}{3}}\left(\psi_{1,-1} - \psi_{1,-1}, -i(\psi_{1,-1} + \psi_{1,-1}), \sqrt{2}\psi_{1,0}\right)\,. \tag{6.11}$$

The function $\boldsymbol{\varepsilon}_0(\mathbf{r},t)$ and the vector $\boldsymbol{\varepsilon}_1(\mathbf{r},t)$ embody the first two orders of the expansion of the source term (Eq. 6.5), similarly to ψ and $\mathbf{J}$ for L. Eqs. (6.9) and (6.10) are known as the P_1 equations and constitute the starting point to derive the diffusion equation (DE). The DE is considered valid at macroscopic length scales[2] (Van Rossum and Nieuwenhuizen, 1999) and derived under the assumption that the radiance has a weak angular dependence, originated by a high albedo scattering medium, i.e. $\mu_a \ll \mu_s$ (Wang and Wu, 2007). To derive the DE, $\mathbf{J}(\mathbf{r},t)$ is algebraically eliminated from Eq. (6.9) by using Eq. (6.10) under the condition known as the diffusion approximation (DA) (Wang and Wu, 2007)

$$\tau_0\left|\frac{\partial}{\partial t}\mathbf{J}(\mathbf{r},t)\right| \ll |\mathbf{J}(\mathbf{r},t)|\,, \quad \tau_0 = \frac{\eta}{c\left[\mu_a(\mathbf{r}) + \mu'_{\mathrm{s}}(\mathbf{r})\right]}\,. \tag{6.12}$$

The DA imposes constraints on the relative time variation of $\mathbf{J}(\mathbf{r},t)$, which contains the odd-order first terms of the series in Eq. (6.4). If in addition to the DA, we have an isotropic source distribution, then $\boldsymbol{\varepsilon}_1(\mathbf{r},t) = \mathbf{0}$, and the classical DE is obtained (Wang and Wu, 2007)

$$\frac{\eta}{c}\frac{\partial\phi_0(\mathbf{r},t)}{\partial t} + \nabla\cdot\left[D(\mathbf{r})\nabla\phi_0(\mathbf{r},t)\right] + \mu_a(\mathbf{r})\phi_0(\mathbf{r},t) = \varepsilon_0(\mathbf{r},t)\,, \tag{6.13}$$

where $D(\mathbf{r})$ is the standard diffusion coefficient

$$D(\mathbf{r}) = \frac{1}{3\left[\mu_a(\mathbf{r}) + \mu'_{\mathrm{s}}(\mathbf{r})\right]} \approx \frac{1}{3\mu'_{\mathrm{s}}(\mathbf{r})}\,, \tag{6.14}$$

and the inequality $\mu_a \ll \mu_s$ has been used to approximate the diffusion coefficient. Next, we introduce an approximation to the RTE similar to the P_N approximation: the simplified spherical harmonics approximation.

6.3 The simplified spherical harmonics approximation

Additionally to the time variable (or modulation frequency if FD methods are used), the radiation field is position and direction-dependent. Thus, elaborating numerical schemes for solving the RTE may involve a discretization method for

[2] Length scales such as $\lambda \ll l'_{tr} \ll l_s$, where λ is the wavelength, l'_{tr} the transport mean free path and l_s the sample size.

up to a six-dimensional space. For this reason, RTE approximations that preserve enough accuracy while reducing computation time are highly desirable for practical applications. That is the purpose of low-order transport models such as the P_N approximation (Arridge, 1999; Wright et al. 2007). However, the large number and complexity of the P_N equations (as an extra feature, mixed spatial derivatives are contained in the equations) limit the applicability of the P_N approximation. An alternative is the simplified P_N (SP_N) approximation which transforms the RTE into a system of coupled diffusion equations (elliptic in the steady-state case or parabolic in the time-dependent case) that depend solely on space and time (Klose and Larsen, 2006). The SP_N equations display a significantly reduced complexity compared to the P_N equations, and allow the application of DE-like numerical schemes and solvers (Klose and Larsen, 2006; Chu et al., 2009; Bouza Domínguez and Bérubé-Lauzière, 2010, Montejo et al., 2011).

Applying the SP_N approximation, a methodology coined the SP_N method, originated in the field of nuclear reactor theory (Fletcher, 1983; de Oliveira, 1986). In its early days, the SP_N method lacked firm theoretical foundations, which hampered its use. Further developments allowed resolving this issue and expanding the applications of the SP_N equations to other fields such as heat transport (Larsen et al., 2002), coupled electron–photon transport problems (Kotiluoto et al., 2007), and biomedical optics (Klose and Larsen, 2006).

The SP_N equations have been derived in three ways: (*i*) as a multidimensional generalization of the P_N equations for geometries with planar symmetry – so-called the formal or heuristic derivation (Gelbard, 1960), (*ii*) as an asymptotic correction to the diffusion approximation (Larsen et al., 1996) and (*iii*) using a rigorous variational analysis approach (Tomasevic and Larsen, 1996; Brantley and Larsen, 2000). In biomedical optics, it has been demonstrated that SP_N equations provide transport-like solutions for modeling visible and near-infrared light propagation in small tissue geometries and specially, in the presence of high absorption ($\sim 1\,\mathrm{cm}^{-1}$) (Klose and Larsen, 2006). In addition, these results are achieved with only a fraction of the computational cost of a transport calculation and a minimum of twice the cost of DE calculations (Klose and Larsen, 2006). Moreover, SP_N equations have been introduced in luminescence imaging and provided the inherent advantages of transport-like solutions in model-based image reconstruction algorithms (Klose, 2009; Klose, 2012).

Subsequently, we first present the heuristic derivation of the SP_N equations and corresponding boundary conditions based on the planar symmetry assumption for time-independent problems arising in biomedical optics (the more rigorous derivation based on variational analysis is not discussed here as it would require too much space, and is beyond the scope of the present work). Following this, we will discuss the SP_N equations for the frequency and time domains.

6.3.1 The steady-state SP_N equations

For deriving the SP_N equations, we will assume that the optical properties of the medium vary only along a given axis, and not along directions perpendicular to this axis (i.e., we have a medium with planar symmetry). This also assumes that there is azimuthal symmetry (i.e. no dependence on the spherical angle ϕ, see Fig. 6.2). The

z axis will then be called the axis of symmetry. For a medium with such symmetry, the time-independent RTE (or the equivalent, in terms of the diffuse component of the radiance) has the following form (Klose and Larsen, 2006)

$$\varpi \frac{\partial}{\partial z}\psi(z,\varpi) = -\left[\mu_{\mathrm{a}}(z)+\mu_{\mathrm{s}}(z)\right]\psi\left(z,\varpi\right) + \int_{-1}^{1} \widetilde{\mu}_{\mathrm{s}}(z,\varpi,\varpi')\psi\left(z,\varpi'\right)\,\mathrm{d}\varpi' + \frac{Q(z)}{2}\,, \tag{6.15}$$

where $\psi(z,\varpi)$ can be either the radiance $L(z,\varpi)$ for a medium with embedded isotropic sources or its diffuse radiance component, z is the coordinate along the axis of symmetry oriented along the unit vector $\widehat{\mathbf{k}}$ and $\varpi = \widehat{\mathbf{s}}\cdot\widehat{\mathbf{k}}$ is the cosine of the angle between a given direction of propagation $\widehat{\mathbf{s}}$ and $\widehat{\mathbf{k}}$, $\widetilde{\mu}_{\mathrm{s}}(z,\varpi,\varpi') = \mu_{\mathrm{s}}p(z,\varpi,\varpi')$ is the differential scattering coefficient (or modified phase function) and $Q(z)$ represents a time-independent isotropic source.

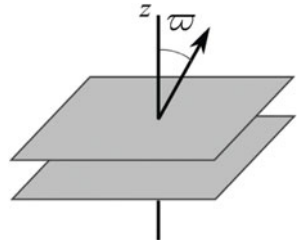

Fig. 6.2. Planar symmetry in a medium.

The corresponding boundary condition is

$$\psi(z,\varpi) = B_T(z,\varpi) + R_F(\varpi)\psi(z,-\varpi)\,, \quad z\in S,\ 0<\varpi<1\,, \tag{6.16}$$

where for the diffuse component of the radiance, we can simply assume that $B_T(z,\varpi)=0$. If we integrate Eq. (6.15) over the interval $[-1,1]$, we obtain the exact equation

$$\frac{\mathrm{d}\psi_1(z)}{\mathrm{d}z} = -\mu_{\mathrm{a}}(z)\psi_0(z) + \frac{Q(z)}{2}\,, \tag{6.17}$$

where $\psi_0(z)$ and $\psi_1(z)$ are the fluence and the radiant current density for a medium with planar symmetry. In addition, they are the zeroth and first moments of the Legendre expansion of $\psi(z,\varpi)$ (see below the radiance Legendre expansion).

We may develop the modified phase function $\widetilde{\mu}_{\mathrm{s}}(z,\varpi,\varpi')$ and $\psi\left(z,\varpi\right)$ along Legendre polynomials as follows (we assume that $\widetilde{\mu}_{\mathrm{s}}(z,\varpi,\varpi') = \widetilde{\mu}_{\mathrm{s}}(z,\varpi\cdot\varpi')$, i.e. that scattering only depends on the angle between the incident and scattered directions)

$$\widetilde{\mu}_{\mathrm{s}}(z,\varpi,\varpi') = \sum_{n=0}^{\infty}\left(\frac{2n+1}{2}\right)\mu_s(z)g_n(z)P_n(\varpi)P_n\left(\varpi'\right)\,, \tag{6.18}$$

$$\psi\left(z,\varpi\right) = \sum_{n=0}^{\infty}\left(\frac{2n+1}{2}\right)\psi_n(z)P_n(\varpi)\,. \tag{6.19}$$

where $g_n(z)$ and $\psi_n(z)$ are the Legendre moments of the phase function and radiance, respectively. In the case of the Henyey–Greenstein phase function, $g_n(z) = [g(z)]^n$, where g describes the possibly space-dependent degree of anisotropy of the scattering (the anisotropy parameter).

Substituting the Legendre expansions into the main equation for $\psi(z, \varpi)$, multiplying both sides by $P_{n'}(\varpi)$, $n \neq 0$, and integrating over the interval $[-1, 1]$, we obtain

$$\mu_n(z)\psi_n(z) + \frac{\mathrm{d}}{\mathrm{d}z}\left[\frac{n+1}{2n+1}\psi_{n+1}(z) + \frac{n}{2n+1}\psi_{n-1}(z)\right] = 0\,, \quad n = 1, \ldots, \infty\,, \tag{6.20}$$

where the orthogonality property and the recurrence relation of the Legendre polynomials have been used (Abramowitz and Stegun, 1965). Here, we defined the nth-order transport coefficients as $\mu_n(z) = \mu_a(z) + \mu_s(z)[1 - g_n(z)]$. The former equation allows expressing the moments $\psi_n(z)$ as

$$\psi_n(z) = -\frac{1}{\mu_n(z)}\frac{\mathrm{d}}{\mathrm{d}z}\left[\frac{n+1}{2n+1}\psi_{n+1}(z) + \frac{n}{2n+1}\psi_{n-1}(z)\right]. \tag{6.21}$$

If the Legendre expansion of the radiance given in Eq. (6.19) is truncated at a given order N, which can be selected to be odd, the *odd-order P_N equations* for planar geometries are obtained. Next, we employ Eqs. (6.21) to algebraically eliminate the odd-order moments. After some algebra, we obtain final equations for the even-order moments

$$\begin{aligned}
&\mu_n(z)\psi_n(z) - \frac{n+1}{2n+1}\frac{\mathrm{d}}{\mathrm{d}z}\left\{\frac{1}{\mu_{n+1}(z)}\frac{\mathrm{d}}{dz}\left[\frac{n+2}{2n+3}\psi_{n+2}(z) + \frac{n+1}{2n+3}\psi_n(z)\right]\right\} \\
&\quad - \frac{n}{2n+1}\frac{\mathrm{d}}{\mathrm{d}z}\left\{\frac{1}{\mu_{n-1}(z)}\frac{\mathrm{d}}{\mathrm{d}z}\left[\frac{n}{2n-1}\psi_n(z) + \frac{n-1}{2n-1}\psi_{n-2}(z)\right]\right\} = \delta_{n,0}Q(z)\,, \\
&\quad n = 0, 2, \ldots, N-1\,.
\end{aligned} \tag{6.22}$$

Eq. (6.22) is a system of $K = (N+1)/2$ coupled one-dimensional elliptic equations with K unknowns $\{\psi_n(z)\}_{i=0,2,\ldots,N-1}$, K being even. As mentioned before, odd-order moments can be obtained from the solution of Eq. (6.22) and back-substitution in Eq. (6.21), up to the truncated order N.

The extension of Eq. (6.22) to the three-dimensional case is obtained by replacing z by $\mathbf{r}$, and substituting each operator by its 3-D counterpart in 3-D, i.e. the partial derivative $\partial/\partial z$ becomes the gradient operator $\nabla \equiv [\partial/\partial x,\ \partial/\partial y,\ \partial/\partial z]$. Here, the second angular dependence of the spherical harmonics expansion (the generalization of the P_N approximation for 3-D) is neglected. The final simplified P_N equations (SP_N equations) for steady-state 3-D problems are thus

$$\begin{aligned}
&\mu_n(\mathbf{r})\psi_n(\mathbf{r}) - \frac{n+1}{2n+1}\nabla\cdot\left\{\frac{1}{\mu_{n+1}(\mathbf{r})}\nabla\left[\frac{n+2}{2n+3}\psi_{n+2}(\mathbf{r}) + \frac{n+1}{2n+3}\psi_n(\mathbf{r})\right]\right\} \\
&\quad - \frac{n}{2n+1}\nabla\left\{\frac{1}{\mu_{n-1}(\mathbf{r})}\nabla\left[\frac{n}{2n-1}\psi_n(\mathbf{r}) + \frac{n-1}{2n-1}\psi_{n-2}(\mathbf{r})\right]\right\} = \delta_{n,0}Q(\mathbf{r}), \\
&\quad n = 0, 2, \ldots, N-1\,.
\end{aligned} \tag{6.23}$$

Because of the approximations performed in deriving Eq. (6.23), the solution of the SP_N equations Eq. (6.23) does not converge to the exact transport solution (see Eqs. (6.15)) as $N \to \infty$. Instead, the solution of Eq. (6.23) converges asymptotically to the transport solution so there is an optimal order N for each physical situation (Klose and Larsen, 2006).

To simplify the notation, it is convenient to rewrite Eq. (6.23) in matrix format. For this, we introduce the column vector of even-order moments $\mathbf{\Psi}(\mathbf{r}) = [\psi_{k'}(\mathbf{r})]^T$, $k' = 0, 2, 4, \ldots, N-1$, which is in turn rewritten in terms of the vector of composite moments $\mathbf{\Phi}(\mathbf{r}) = [\varphi_k(\mathbf{r})]^T$, $k = 1, \ldots, K$. The relationship between the even-order moments and the composite moments, and its inverse, can be expressed in a convenient matrix notation. Up to $N = 7$ (higher orders can be obtained as well from Eq. (6.23)), this relationship is given by

$$\mathbf{\Psi}(\mathbf{r}) = \mathbf{T}\mathbf{\Phi}(\mathbf{r}), \quad \mathbf{\Phi}(\mathbf{r}) = \mathbf{T}^{-1}\mathbf{\Psi}(\mathbf{r}), \quad \text{where } \mathbf{T}^{-1} = \begin{bmatrix} 1 & 2 & 0 & 0 \\ 0 & 3 & 4 & 0 \\ 0 & 0 & 5 & 6 \\ 0 & 0 & 0 & 7 \end{bmatrix}.$$

The composite moments allow diagonalizing the 'diffusive operator' containing the differential operators having the form $-\nabla \cdot (D_K \nabla)$. This leads to the matrix form of the steady-state SP_N equations (or CW-SP_N model)

$$(D_r + \mathbf{C})\mathbf{\Phi}(\mathbf{r}) = \mathbf{Q}(\mathbf{r}). \tag{6.24}$$

The term D_r is a diagonal $K \times K$ matrix operator whose elements are all on the main diagonal and given by

$$\operatorname{diag}_{(0)}(D_r) = \begin{bmatrix} -\nabla \cdot (D_1 \nabla) & -\nabla \cdot (D_2 \nabla) & \cdots & -\nabla \cdot (D_K \nabla) \end{bmatrix}, \quad k = 1, \ldots, K, \tag{6.25}$$

where $D_k = 1/[(4k-1)\mu_{2k-1}]$ and the expression $\operatorname{diag}_{(0)}(\ )$ denotes the list of the main diagonal elements. Note that we use index (0) for the main diagonal and positive (negative) values for diagonals located under (below) the main diagonal (such notation will be used again in the sequel). The components of the (symmetric) matrix $\mathbf{C}$ are linear combinations of the transport coefficients μ_n. The explicit expressions for the columns of $\mathbf{C}$ in Matlab notation (up to $N = 7$) are given by

$$\mathbf{C}(:, 1) = \begin{bmatrix} \mu_0(\mathbf{r}) \\ -\frac{2}{3}\mu_0(\mathbf{r}) \\ \frac{8}{15}\mu_0(\mathbf{r}) \\ -\frac{16}{35}\mu_0(\mathbf{r}) \end{bmatrix}, \quad \mathbf{C}(:, 2) = \begin{bmatrix} -\frac{2}{3}\mu_0(\mathbf{r}) \\ \frac{4}{9}\mu_0(\mathbf{r}) + \frac{5}{9}\mu_2(\mathbf{r}) \\ -\frac{16}{45}\mu_0(\mathbf{r}) - \frac{4}{9}\mu_2(\mathbf{r}) \\ \frac{32}{105}\mu_0(\mathbf{r}) + \frac{8}{21}\mu_2(\mathbf{r}) \end{bmatrix},$$

$$\mathbf{C}(:,3)=\begin{bmatrix}\frac{8}{15}\mu_0(\mathbf{r})\\ -\frac{16}{45}\mu_0(\mathbf{r})-\frac{4}{9}\mu_2(\mathbf{r})\\ \frac{64}{225}\mu_0(\mathbf{r})+\frac{16}{45}\mu_2(\mathbf{r})+\frac{9}{25}\mu_4(\mathbf{r})\\ -\frac{128}{525}\mu_0(\mathbf{r})-\frac{32}{105}\mu_2(\mathbf{r})-\frac{54}{175}\mu_4(\mathbf{r})\end{bmatrix},$$

$$\mathbf{C}(:,4)=\begin{bmatrix}-\frac{16}{35}\mu_0(\mathbf{r})\\ \frac{32}{105}\mu_0(\mathbf{r})+\frac{8}{21}\mu_2(\mathbf{r})\\ -\frac{128}{525}\mu_0(\mathbf{r})-\frac{32}{105}\mu_2(\mathbf{r})-\frac{54}{175}\mu_4(\mathbf{r})\\ \frac{256}{1225}\mu_0(\mathbf{r})+\frac{64}{245}\mu_2(\mathbf{r})+\frac{324}{1225}\mu_4(\mathbf{r})+\frac{13}{49}\mu_6(\mathbf{r})\end{bmatrix}. \tag{6.26}$$

The column vector $\mathbf{Q}(\mathbf{r})$ contains the information about the source; it is given by

$$\mathbf{Q}(\mathbf{r})=Q(\mathbf{r})\begin{bmatrix}1 & -\frac{2}{3} & \frac{8}{15} & -\frac{16}{35}\end{bmatrix}^T. \tag{6.27}$$

6.3.2 SP_N boundary conditions and measurement modeling

The boundary conditions (BCs) associated with Eq. (6.24) can be obtained by inserting Eq. (6.19) into Eq. (6.16) and carrying out integrations similarly to what was done previously. In a convenient matrix form, these BCs are

$$\mathbf{A}\mathbf{\Phi}(\mathbf{r})+\mathbf{B}\frac{\partial}{\partial\widehat{\mathbf{n}}}\mathbf{\Phi}(\mathbf{r})=\mathbf{S}(\mathbf{r}),\quad \mathbf{r}\in\partial V, \tag{6.28}$$

where $\partial/\partial\widehat{\mathbf{n}}$ denotes the derivative along the outward-pointing normal $\widehat{\mathbf{n}}$ to the boundary. The boundary matrices $\mathbf{A}$, $\mathbf{B}$ and vector $\mathbf{S}$ (external source vector) depend on the reflectivity properties of the boundary and the optical coefficients of the medium. We assume $\mathbf{S}=\mathbf{0}$ for SP_N equations originated from the RTE in terms of the diffuse component of the radiance, since it is related to the exterior source. The mentioned terms have the following form (up to $N=7$)

$$\mathbf{A}=\begin{bmatrix}1/2+A_1 & -1/8-C_1 & 1/16-E_1 & -5/128-G_1\\ -1/8-C_2 & 7/24+A_2 & -41/384-E_2 & 1/16-G_2\\ 1/16-C_3 & -41/384-E_3 & 407/1920+A_3 & -233/2560-G_3\\ -5/128-C_4 & 1/16-E_4 & -233/2560-G_4 & 3023/17920+A_4\end{bmatrix}, \tag{6.29}$$

$$\mathbf{B}=\begin{bmatrix}(1+B_1)/3\mu_1 & -D_1/\mu_3 & -F_1/\mu_5 & -H_1/\mu_7\\ -D_2/3\mu_1 & (1+B_2)/7\mu_3 & -F_2/\mu_5 & -H_2/\mu_7\\ -D_3/3\mu_1 & -F_3/\mu_3 & (1+B_3)/11\mu_5 & -H_3/\mu_7\\ -D_4/3\mu_1 & -F_4/\mu_3 & -H_4/\mu_5 & (1+B_4)/15\mu_7\end{bmatrix}. \tag{6.30}$$

$$\mathbf{S} = \begin{bmatrix} \displaystyle\int_{\widehat{\mathbf{s}}\cdot\widehat{\mathbf{n}}>0} B_T(\mathbf{r},\widehat{\mathbf{s}}) 2\,|\widehat{\mathbf{s}}\cdot\widehat{\mathbf{n}}|\;\mathrm{d}\Omega \\ \displaystyle\int_{\widehat{\mathbf{s}}\cdot\widehat{\mathbf{n}}>0} B_T(\mathbf{r},\widehat{\mathbf{s}}) \left[5|\widehat{\mathbf{s}}\cdot\widehat{\mathbf{n}}|^3 - 2\,|\widehat{\mathbf{s}}\cdot\widehat{\mathbf{n}}|\right]\mathrm{d}\Omega \\ \displaystyle\int_{\widehat{\mathbf{s}}\cdot\widehat{\mathbf{n}}>0} B_T(\mathbf{r},\widehat{\mathbf{s}}) \left[\frac{63}{4}|\widehat{\mathbf{s}}\cdot\widehat{\mathbf{n}}|^5 - \frac{35}{2}|\widehat{\mathbf{s}}\cdot\widehat{\mathbf{n}}|^3 + \frac{15}{4}\,|\widehat{\mathbf{s}}\cdot\widehat{\mathbf{n}}|\right]\mathrm{d}\Omega \\ \displaystyle\int_{\widehat{\mathbf{s}}\cdot\widehat{\mathbf{n}}>0} B_T(\mathbf{r},\widehat{\mathbf{s}}) \left[\frac{429}{8}|\widehat{\mathbf{s}}\cdot\widehat{\mathbf{n}}|^7 - \frac{693}{8}|\widehat{\mathbf{s}}\cdot\widehat{\mathbf{n}}|^5 + \frac{315}{8}|\widehat{\mathbf{s}}\cdot\widehat{\mathbf{n}}|^3 - \frac{35}{8}\,|\widehat{\mathbf{s}}\cdot\widehat{\mathbf{n}}|\right]\mathrm{d}\Omega \end{bmatrix}, \tag{6.31}$$

where the coefficients $(A_1,\ldots,H_1,\ A_4,\ldots,H_4)$ (see Appendix A of Klose and Larsen (2006) for their explicit expressions) are linear combinations of the angular moments $R_{F,n}$ of the angle-dependent Fresnel coefficient R_F

$$R_{F,n} = \int_0^1 x^n R_F(x)\,\mathrm{d}x\,. \tag{6.32}$$

The Robin-type boundary condition Eq. (6.28) can be considered as the Marshak condition (Davidson and Sykes, 1957) for the vector of composite moments at a tissue–air interface, where Fresnel reflections occurs. For $N = 1$, Eq. (6.28) becomes the common Robin (or Marshak) boundary condition for the DE (Marshak, 1947; Ishimaru, 1978). At tissue–tissue interfaces, the normal component of the radiant current density vector $J_{no} = \mathbf{J}(\mathbf{r},t)\cdot\widehat{\mathbf{n}}$ is continuous (we can just add both equations appearing in Eq. (6.3)). Then, corresponding boundary conditions can be found by mere substitution of the expansion Eq. (6.19) in this condition and grouping of similar terms.

To end up with the derivation of the SP_N equations as a forward model in inverse problems, we need an expression for relating the outgoing light to the vector of composite moments $\mathbf{\Phi}(\mathbf{r})$. If we take as measurements a finite collection of exitance values (outgoing normal component of the radiant current density vector) $J_{no}^{(out)}$, then

$$J_{no}^{(out)} = \left[\mathbf{j}_1 - \mathbf{j}_2(\mathbf{B})^{-1}\mathbf{A}\right]\mathbf{\Phi}\left(\mathbf{r}_d,t\right) = \mathbf{V}_\mu\mathbf{\Phi}\left(\mathbf{r}_d,t\right)\,, \tag{6.33}$$

where $\mathbf{V}_\mu$ is the measurement operator (vector) that depends on the optical properties of the medium, $\mathbf{r}_d$ is a position where a measurement is made ('detector position'), and the vectors $\mathbf{j}_1$ and $\mathbf{j}_2$ have the following expressions (up to $N = 7$)

$$\mathbf{j}_1 = \begin{bmatrix} 1/4 + J_0 \\ (1/4+J_0)\,(-2/3) + (5/16+J_2)\,(1/3) \\ (1/4+J_0)\,(8/15) + (5/16+J_2)\,(-4/15) + (-3/32+J_4)\,(1/5) \\ (1/4+J_0)\,(-15/35) + (5/16+J_2)\,(8/35) + (-3/32+J_4)\,(-6/35) + (13/256+J_6)\,(1/7) \end{bmatrix}^T, \tag{6.34}$$

$$\mathbf{j}_2 = \left[-\left(\frac{0.5+J_1}{3\mu_1}\right),\quad \left(-\frac{J_3}{7\mu_3}\right),\quad \left(-\frac{J_5}{11\mu_5}\right),\quad \left(-\frac{J_7}{15\mu_7}\right)\right]. \tag{6.35}$$

The coefficients $(J_0, J_1, \ldots)$ depend on the angular moments of the angle-dependent Fresnel reflection coefficient $R_{F,n}$ (Eq. (6.32)), and can be found in (Klose and Larsen, 2006).

The SP_N equations Eqs. (6.24) along with their boundary conditions – Eq. (6.28) have been numerically implemented and compared with DE-based and transport (RTE-based) calculations (Klose and Larsen, 2006). The calculations are performed in small homogeneous geometries: $1 \times 1\,\mathrm{cm}$ and $2 \times 2\,\mathrm{cm}$, that mimic a tomographic slice of a small animal. The absorption coefficient values are taken from 0.01 to $2\,\mathrm{cm}^{-1}$ (high absorption). The reduced scattering coefficient is kept constant as $10\,\mathrm{cm}^{-1}$ but considering a variation of the scattering coefficient from 10 to $50\,\mathrm{cm}^{-1}$ and the anisotropy factor g from 0 to 0.8. In every case, a medium with a refractive index value of $\eta = 1.37$ is considered as surrounded by air. In a second round, numerical experiments are carried out in a $2 \times 2\,\mathrm{cm}$ diffusive medium with $\mu_a = 0.01\,\mathrm{cm}^{-1}$, $\mu_s = 10\,\mathrm{cm}^{-1}$, $g = 0$ and non-reentry boundary conditions $\eta = 1$. Highly absorbing inclusions ($\mu_a = 2\,\mathrm{cm}^{-1}$) are embedded in the diffusive medium. Following an analysis of the experiment results, see (Klose and Larsen, 2006) for details, the authors concluded that the SP_N equations Eqs. (6.24) (*i*) can accurately model light propagation in small tissue geometries at visible and near-infrared wavelengths, (*ii*) provide transport-like solutions with a considerably reduced computational cost in comparison with RTE-based calculations and (*iii*) improve DE solutions in transport-like domains with high absorption and small geometries.

6.3.3 Analytical solutions

Analytical solutions are essential for experiments with simple geometries and validation of numerical approaches. Recently, steady-state analytical solutions have been found for infinite (SP_3 and SP_5 equations) and semi-infinite (SP_3 equations) homogeneous media (Liemert and Kienle, 2010; Liemert and Kienle, 2011a). In addition, a methodology for the generalization of the results to the frequency- and time-domain cases is suggested. The final expressions for the composite moments are set out as linear combinations of DE free space Green's functions. Next, we write down the main results for the aforementioned geometries.

6.3.3.1 Infinite homogeneous medium

An infinite homogeneous medium with an isotropic point source located at the origin of coordinates $Q(\mathbf{r}) = \delta(r)/4\pi r^2$ (r is the distance from the source location) has an inherent spherical symmetry. This symmetry allows the following spherical wave expansion of the composite moments and the source

$$\varphi_i(r) = \frac{1}{2\pi^2 r} \int_0^\infty p\, \widehat{\varphi}_i(p)\, \sin(pr)\, \mathrm{d}p\,, \quad i = 1, 2 \tag{6.36}$$

$$Q(r) = \frac{1}{2\pi^2 r} \int_0^\infty p\, \sin(pr)\, \mathrm{d}p\,, \quad i = 1, 2 \tag{6.37}$$

where the hat over a quantity means the transformed quantity in the p-space. Introducing Eqs. (6.36) and (6.37) into Eq. (6.24) leads to the following system of

linear equations

$$L(\mu_n, p)\widehat{\mathbf{\Phi}}(p) = \widehat{\mathbf{Q}}\,, \tag{6.38}$$

where $\widehat{\mathbf{Q}} = [1 - 2/3]^T$ and $L\,(\mu_n, p)$ is a matrix whose coefficients depend on the optical properties of the medium (μ_n) and p. For $N = 3$ (hereon, following (Liemert and Kienle, 2010), we show results for $N = 3$ and 5 only) we get

$$L\,(\mu_n, p) = \begin{bmatrix} p^2/3\mu_1 + \mu_a & -2\mu_a/3 \\ -2\mu_a/3 & p^2/7\mu_3 + 4\mu_a/9 + 5\mu_2/9 \end{bmatrix}. \tag{6.39}$$

From Eq. (6.38), the composite moment functions $\widehat{\varphi}_i(p)$, $i = 1, 2$ are determined as the ratio of even-order polynomials in p

$$\widehat{\varphi}_i(p) = \begin{cases} \dfrac{F_i^{(1)}(p^2)}{p^4 + \alpha p^2 + \beta}, & i = 1, 2, \text{ for } N = 3 \\ \dfrac{F_i^{(2)}(p^2)}{p^6 + \alpha p^4 + \beta p^2 + \gamma}, & i = 1, 2, 3 \text{ for } N = 5 \end{cases}, \; F_i^{(m)}(x) = \sum_{j=i-1}^{m} a_{ij} x^j\,, \tag{6.40}$$

where the coefficients a_{ij} appearing in the definition of the polynomial $F_i^{(m)}(x)$ are given by

$$a_{10} = \frac{35}{3}\mu_1\mu_2\mu_3\,, \quad a_{11} = 3\mu_1\,, \quad a_{21} = -\frac{14}{3}\mu_3\,, \quad \text{for } N = 3\,, \tag{6.41}$$

$$a_{10} = \frac{231}{5}\mu_1\mu_2\mu_3\mu_4\mu_5\,, \quad a_{11} = \frac{35}{3}\mu_1\mu_2\mu_3 + 33\mu_1\mu_5\left(\frac{16}{45}\mu_2 + \frac{9}{25}\mu_4\right), \quad a_{12} = 3\mu_1\,,$$
$$a_{21} = -\frac{462}{25}\mu_3\mu_4\mu_5\,, \quad a_{22} = -\frac{14}{3}\mu_3\,, \quad a_{32} = \frac{88}{15}\mu_5\,, \qquad \text{for } N = 5\,. \tag{6.42}$$

The coefficients α, β and γ for the polynomials of the denominator are real positive numbers that depend on the transport coefficients

$$\alpha = 3\mu_a\mu_1 + \frac{28}{9}\mu_a\mu_3 + \frac{35}{9}\mu_2\mu_3\,, \quad \beta = \frac{35}{3}\mu_a\mu_1\mu_2\mu_3\,, \quad \text{for } N = 3\,, \tag{6.43}$$

$$\alpha = 3\mu_a\mu_1 + \frac{28}{9}\mu_a\mu_3 + \frac{35}{9}\mu_2\mu_3 + 11\mu_5\left(\frac{64}{225}\mu_a + \frac{16}{45}\mu_2 + \frac{9}{25}\mu_4\right),$$
$$\beta = \mu_a\mu_1\left(\frac{35}{3}\mu_2\mu_3 + \frac{176}{15}\mu_2\mu_5 + \frac{297}{25}\mu_4\mu_5\right) + \mu_3\mu_4\mu_5\left(\frac{308}{25}\mu_a + \frac{77}{5}\mu_2\right),$$
$$\gamma = \frac{231}{5}\mu_a\mu_1\mu_2\mu_3\mu_4\mu_5\,, \quad \text{for } N = 5\,. \tag{6.44}$$

For $N = 3$, using the expressions for α and β given in Eq. (6.49), it can be shown that the polynomial discriminant $\sqrt{\alpha^2 - 4\beta}$ of the denominator in Eq. (6.40)

is always positive. Therefore, a partial fractions expansion using the polynomial zeros $\lambda_{1,2} = \left(-\alpha \pm \sqrt{\alpha^2 - 4\beta}\right)/2$ is possible. Thus, the composite moments can be written as

$$\widehat{\varphi}_i(p) = \frac{A_i}{p^2 + p_1^2} + \frac{B_i}{p^2 + p_2^2}\,, \quad p_j = \sqrt{-\lambda_j}\,, \quad j = 1, 2\,, \tag{6.45}$$

where

$$A_i = \frac{F_i^{(1)}(\lambda_1)}{k_2^2 - k_1^2}\,, \quad B_i = -\frac{F_i^{(1)}(\lambda_2)}{k_2^2 - k_1^2}\,. \tag{6.46}$$

In the case of an infinite medium, it is known that the Green's function $G(r)$ of the steady-state DE is given by

$$\begin{aligned} G(r) &= \frac{e^{-\mu_{eff} r}}{4\pi D r} = \frac{1}{2\pi^2 r}\int_0^\infty \frac{p\,\sin(pr)}{p^2 + \mu_{eff}}\,\mathrm{d}p\,, \\ D &= \frac{1}{3\left(\mu_a + \mu'_{\mathrm{s}}\right)}\,, \quad \mu_{eff} = \sqrt{3\mu_a(\mu_a + \mu'_{\mathrm{s}})}\,. \end{aligned} \tag{6.47}$$

A comparison of Eqs. (6.45) and (6.47) shows that the composite moment functions $\varphi_i(r)$, $i = 1, 2$ can be written as a superposition of two DE free space Green's functions $G(r)$ as follows

$$\varphi_i(r) = A_i \frac{e^{-p_1 r}}{4\pi r} + B_i \frac{e^{-p_2 r}}{4\pi r}\,, \quad p_j = \sqrt{-\lambda_j}\,, \quad j = 1, 2\,. \tag{6.48}$$

Similarly, for $N = 5$ the polynomial appearing in the denominator of Eq. (6.40) can be decomposed into three partial fractions. It is thus possible to demonstrate that each composite moment function can be expanded into three DE free space Green's functions $G(r)$ as

$$\varphi_i(r) = A_i \frac{e^{-p_1 r}}{4\pi r} + B_i \frac{e^{-p_2 r}}{4\pi r} + C_i \frac{e^{-p_3 r}}{4\pi r}\,, \quad p_j = \sqrt{-\lambda_j}\,, \quad j = 1, 2, 3, \tag{6.49}$$

where the expressions for the expansion coefficients are

$$\begin{aligned} A_i &= \frac{F_i^{(2)}(\lambda_1)}{\left(p_2^2 - p_1^2\right)\left(p_3^2 - p_1^2\right)}\,, \quad B_i = -\frac{F_i^{(2)}(\lambda_2)}{\left(p_2^2 - p_1^2\right)\left(p_3^2 - p_2^2\right)}\,, \\ C_i &= \frac{F_i^{(2)}(\lambda_3)}{\left(p_3^2 - p_1^2\right)\left(p_3^2 - p_2^2\right)}\,, \quad p_j = \sqrt{-\lambda_j}\,,\ j = 1, 2, 3\,. \end{aligned} \tag{6.50}$$

The zeros of polynomials λ_j appearing in Eq. (6.50) can be calculated from Viète's trigonometric method for obtaining roots of third-degree polynomials as (see Liemert and Kienle, 2010)

$$\begin{aligned} \lambda_j &= 2\sqrt{\frac{\xi}{3}}\,\cos\left[\frac{\nu + 2(j-1)\,\pi}{3}\right]\,, \quad \xi = \frac{1}{3}\alpha^2 - \beta\,, \\ \nu &= \arccos\left[-\frac{3}{2\xi}\sqrt{\frac{3}{p}}\left(\frac{2}{27}\alpha^3 - \frac{1}{3}\alpha\beta + \gamma\right)\right]\,, \quad j = 1, 2, 3\,. \end{aligned} \tag{6.51}$$

The analytical solutions provided by Eqs. (6.48) and (6.49) are easy to implement. The analog expressions for frequency-domain problems can be calculated by setting $\mu_n(z) = \mu_a(z) + \mu_s(z)\,[1 - g_n(z)] + i(\eta\omega/c)$, where η is the refractive index of the medium, ω is the angular frequency of the intensity modulated source, c is the speed of light in the vacuum and $i = \sqrt{-1}$. By performing the inverse Fourier transform, we can also obtain analytical formulas in time-domain. In the case of the SP_1 (the DE), an analytical formula for time-domain problems can be directly derived (Wang and Wu, 2007).

In (Liemert and Kienle, 2010), Eqs. (6.48) and (6.49) are compared with Monte Carlo simulations (Wang and Wu, 2007) in the steady-state and time domains and with DE solutions. For the steady-state, the numerical experiments are carried out with an infinite homogeneous medium. The optical properties of the medium are $\mu_s' = 1\,\mathrm{mm}^{-1}$, $g = 0.9$ and values of 0.2 and $2\,\mathrm{mm}^{-1}$ are used for the absorption coefficient. An isotropic point source is placed at the origin of coordinates. Then, the steady-state fluence rate versus distance from the isotropic source is calculated using the SP_N and the corresponding DE solutions and simulated using the Monte Carlo method. A comparison of the results showed that the SP_N solutions are in much better agreement that the DE-based solutions with the Monte Carlo simulations. Particularly, the SP_N solutions accurately reproduce Monte Carlo simulations at all distances from the source including both far and very close (<0.5 mm) to the source. In a second set of experiments, the time-resolved reflectance from a semi-infinite scattering medium, with a perpendicular incident pencil beam, is calculated using the SP_N and the DE solutions. The optical properties of the medium are $\mu_s' = 1\,\mathrm{mm}^{-1}$, $g = 0.9$, $\mu_a = 0.1\,\mathrm{mm}^{-1}$ and $\eta = 1.4$. The medium is considered as surrounded by air. The reflectance time-dependence is calculated at distances of 6.5, 9.5, and 12.5 mm from the position where the beam impinges. The results showed that SP_N solutions describe light propagation even for very short time (<100 ps) values, where the DE fails.

6.3.3.2 Semi-infinite homogeneous medium

In this subsection, we present the analytical solution of the SP_N equations for a semi-infinite geometry with an embedded isotropic point source. This solution is due to Liemert and Kienle (Liemert and Kienle, 2011a). Contrary to their approach, we do not use the formalism of bras and kets (i.e. the Dirac formalism of quantum mechanics), which we find less accessible and can be cumbersome to the non-initiated, it is also not absolutely necessary to reach the solution as elementary linear algebra means are sufficient. Although the exposition of the results is carried out for $N = 3$, the methodology presented can be used to achieve similar results for higher orders.

In the present case, the physical situation has an inherent cylindrical symmetry. Thus, we can expand the composite moments and the δ-source distribution using the zero-order Hankel transform

$$\varphi_i(\mathbf{r}) = \frac{1}{2\pi}\int_0^\infty \varphi_i\,(q,z)\,J_0\,(q\rho)\,q\,\mathrm{d}q\,, \quad \delta\,(\mathbf{r}-\mathbf{r}') = \frac{\delta\,(z-z')}{2\pi}\int_0^\infty J_0\,(q\rho)\,q\,\mathrm{d}q\,, \tag{6.52}$$

where $J_0(x)$ is the zeroth-order Bessel function of the first kind. Substituting Eq. (6.52) into Eq. (6.24) yields a system of second order differential equations for $\mathbf{\Phi}(\mathbf{r})$

$$\frac{\mathrm{d}^2\mathbf{\Phi}}{\mathrm{d}z^2} = \left(\mathbf{M}_\mu + q^2\mathbf{I}_{2\times 2}\right)\mathbf{\Phi} + \delta\left(z - z'\right)\boldsymbol{\varepsilon}\,, \tag{6.53}$$

where the coefficient matrix $\mathbf{M}_\mu$ and the vector $\boldsymbol{\varepsilon}$ are

$$\mathbf{M}_\mu = \begin{bmatrix} 3\mu_a\mu_1 & -2\mu_a\mu_1 \\ -14\mu_a\mu_3 & \dfrac{28}{9}\mu_a\mu_3 + \dfrac{35}{9}\mu_2\mu_3 \end{bmatrix}, \quad \boldsymbol{\varepsilon} = \frac{1}{3}\begin{bmatrix} -9\mu_1 \\ 14\mu_3 \end{bmatrix}, \tag{6.54}$$

and $\mathbf{I}_{2\times 2}$ is the 2×2 identity matrix.

The solution of the boundary value problem $\mathbf{\Phi}(q, z)$ posed by Eqs. (6.53) and (6.28) can be obtained by using the superposition principle

$$\mathbf{\Phi}\left(q, z; z'\right) = \mathbf{\Phi}^{(h)}\left(q, z\right) + \mathbf{\Phi}^{(p)}\left(q, z; z'\right)\,, \tag{6.55}$$

where $\mathbf{\Phi}^{(h)}\left(q, z\right)$ is the solution to the source-free problem (homogeneous component) and $\mathbf{\Phi}^{(p)}\left(q, z; z'\right)$ is a particular solution of Eq. (6.53).

The solution to the source-free problem

$$\frac{\mathrm{d}^2\mathbf{\Phi}^{(h)}}{\mathrm{d}z^2} - \left(\mathbf{M}_\mu + q^2\mathbf{I}_{2\times 2}\right)\mathbf{\Phi}^{(h)} = \mathbf{0}\,, \tag{6.56}$$

will be sought in a form with exponential dependence as follows (similarly to scalar ODEs with constant coefficients)

$$\mathbf{\Phi}(q, z) = e^{\lambda(q)z}\mathbf{w}\,, \tag{6.57}$$

with $\mathbf{w}$ a two-component vector independent of q. Inserting this solution into Eq. (6.56) leads to the following

$$\left[\mathbf{M}_\mu - \left(\lambda^2 - q^2\right)\mathbf{I}_{2\times 2}\right]\mathbf{w} = \mathbf{0}\,. \tag{6.58}$$

Hence, for the proposed vector given in Eq. (6.57) to be a solution of the homogeneous equation, $\mathbf{w}$ must be an eigenvector of $\mathbf{M}_\mu$, and $\lambda^2 - q^2$ must be equal to an eigenvalue. At this point, the eigenvalues of $\mathbf{M}_\mu$ must thus be calculated. After some algebra, these are found to be positive (hence they will be denoted by ς_1^2 and ς_2^2), and given by

$$\varsigma_{1/2}^2 = \alpha \pm \sqrt{\alpha^2 - \beta}\,, \tag{6.59}$$

with

$$\alpha = \frac{3}{2}\mu_a\mu_1 + \frac{28}{18}\mu_a\mu_3 + \frac{35}{18}\mu_2\mu_3\,, \quad \beta = \frac{35}{3}\mu_a\mu_1\mu_2\mu_3\,. \tag{6.60}$$

Now that the eigenvalues are found, the associated eigenvectors $\mathbf{w}_1$ and $\mathbf{w}_2$ can be calculated. Let $\mathbf{w}_i = [\xi_i, \eta_i]$, $i = 1, 2$, then ξ_i and η_i must satisfy

$$\left(3\mu_a\mu_1 - \varsigma_i^2\right)\xi_i - \left(2\mu_a\mu_1\right)\eta_i = 0\,. \tag{6.61}$$

Hence $\mathbf{w}_i$ can be taken as follows

$$\mathbf{w}_i = \begin{bmatrix} 2\mu_a\mu_1 \\ 3\mu_a\mu_1 - \varsigma_i^2 \end{bmatrix} . \tag{6.62}$$

The spectral decomposition of $\mathbf{M}_\mu$ will be written as

$$\mathbf{M}_\mu = \mathbf{L}\mathbf{D}\mathbf{L}^{-1} , \tag{6.63}$$

where

$$\mathbf{D} = \operatorname{diag}\left(\varsigma_1^2, \varsigma_2^2\right) , \tag{6.64}$$

and $\mathbf{L}$ has as its columns the eigenvectors $\mathbf{w}_1$ and $\mathbf{w}_2$. These eigenvectors being column vectors, we may thus write

$$\mathbf{L} = [\mathbf{w}_1 \mathbf{w}_2] = \begin{bmatrix} w_{1;1} & w_{2;1} \\ w_{1;2} & w_{2;2} \end{bmatrix} = \begin{bmatrix} 2\mu_a\mu_1 & 2\mu_a\mu_1 \\ 3\mu_a\mu_1 - \varsigma_1^2 & 3\mu_a\mu_1 - \varsigma_2^2 \end{bmatrix} . \tag{6.65}$$

Here $w_{i;j}$ denotes the jth component of vector $\mathbf{w}_i$. Reverting back to λ, we have that $\lambda^2 - q^2$ can be either equal to ς_1^2 or ς_2^2. Hence, there will be 4 possible values for λ, these being $\pm\lambda_i(q)$ with

$$\lambda_i(q) = \sqrt{q^2 + \varsigma_i^2} , \quad i = 1, 2 . \tag{6.66}$$

Now, since we must have $\mathbf{\Phi}^{(h)}(q, z) \to \mathbf{0}$ when $z \to \infty$, we can only retain the possible values of λ, that are negative. Thus, the homogeneous solution can be expressed as the following superposition

$$\mathbf{\Phi}^{(h)}(q, z) = c_1(q)\, e^{-\lambda_1(q) z} \mathbf{w}_1 + c_2(q)\, e^{-\lambda_2(q) z} \mathbf{w}_2 , \tag{6.67}$$

where $c_1(q)$ and $c_2(q)$ will be determined later on using the BCs.

Now, to find the particular solution $\mathbf{\Phi}^{(p)}(q, z; z')$, the following Fourier (or plane wave) decomposition of the particular vector of composite moments, and of the Dirac delta function are used

$$\mathbf{\Phi}^{(p)}(q, z; z') = \frac{1}{2\pi} \int_{-\infty}^{\infty} \mathbf{\Phi}^{(p)}(q, k)\, e^{ik\left(z'-z\right)} \mathrm{d}k , \;\; \delta(z - z') = \frac{1}{2\pi} \int_{-\infty}^{\infty} e^{ik\left(z'-z\right)} \mathrm{d}k . \tag{6.68}$$

Now, recall that $\mathbf{\Phi}^{(p)}(q, z; z')$ must satisfy the following vector differential equation

$$\frac{d^2 \mathbf{\Phi}^{(p)}}{dz^2} - \left(\mathbf{M}_\mu + q^2 \mathbf{I}_{2\times 2}\right) \mathbf{\Phi}^{(p)} = \delta(z - z')\, \boldsymbol{\varepsilon} . \tag{6.69}$$

Inserting the Fourier decompositions into this last equation gives the following linear vector equation

$$\left[\mathbf{M}_\mu + \left(k^2 + p^2\right) \mathbf{I}_{2\times 2}\right] \mathbf{\Phi}^{(p)}(q, k) = -\boldsymbol{\varepsilon} . \tag{6.70}$$

This is similar to the eigenvalue equation encountered before in Eq. (6.58), except that here the left-hand side is not zero. To solve this equation, we use the spectral

decomposition of $\mathbf{M}_\mu$, giving as solution

$$\mathbf{\Phi}^{(p)}(q,k) = \mathbf{L}\left\{\left[\mathbf{D} + \left(k^2+p^2\right)\mathbf{I}_{2\times 2}\right]^{-1}\mathbf{L}^{-1}(-\boldsymbol{\varepsilon})\right\}. \tag{6.71}$$

The quantity in braces is a vector column, and the result on the left-hand side of the last equation is seen to be a linear superposition (or combination) of the columns of $\mathbf{L}$, which are the eigenvectors of $\mathbf{M}_\mu$.[3] $\mathbf{L}$ being a 2×2 matrix, its inverse is easily calculated to be

$$\mathbf{L}^{-1} = \frac{1}{\det(\mathbf{L})}\begin{bmatrix} w_{2;2} & -w_{2;1} \\ -w_{1;2} & w_{1;1}\end{bmatrix}, \tag{6.72}$$

where

$$\det(\mathbf{L}) = 2\mu_a\mu_1\left(\varsigma_1^2 - \varsigma_2^2\right). \tag{6.73}$$

With these last results, the particular solution given in Eq. (6.16) can be more explicitly written as

$$\mathbf{\Phi}^{(p)}(q,k) = \frac{1}{\det(\mathbf{L})}\left(\frac{14\mu_3 w_{2;1} + 9\mu_1 w_{2;2}}{k^2+\lambda_1^2(q)}\mathbf{w}_1 - \frac{14\mu_3 w_{1;1} + 9\mu_1 w_{1;2}}{k^2+\lambda_2^2(q)}\mathbf{w}_2\right). \tag{6.74}$$

Introducing the constants

$$h_1 = \frac{14\mu_3 w_{2;1} + 9\mu_1 w_{2;2}}{3\det(\mathbf{L})}, \quad h_2 = \frac{14\mu_3 w_{1;1} + 9\mu_1 w_{1;2}}{3\det(\mathbf{L})}, \tag{6.75}$$

the last expression for $\mathbf{\Phi}^{(p)}(q,k)$ can more succinctly be written as

$$\mathbf{\Phi}^{(p)}(q,k) = \frac{h_1}{k^2+\lambda_1^2(q)}\mathbf{w}_1 - \frac{h_2}{k^2+\lambda_2^2(q)}\mathbf{w}_2. \tag{6.76}$$

Taking the inverse Fourier transform of the last expression, we get[4]

$$\mathbf{\Phi}^{(p)}(q,z) = \frac{h_1}{2}\frac{e^{-\lambda_1(q)|z-z'|}}{\lambda_1(q)}\mathbf{w}_1 - \frac{h_2}{2}\frac{e^{-\lambda_2(q)|z-z'|}}{\lambda_2(q)}\mathbf{w}_2. \tag{6.77}$$

All the pieces to obtain the complete solution $\mathbf{\Phi}$ decomposed as in Eq. (6.55) have now been found. The use of the BC given in Eq. (6.28) (using that $\widehat{\mathbf{n}} = -\widehat{\mathbf{z}}$) allows determining the constant coefficients $c_1(q)$ and $c_2(q)$ appearing in Eq. (6.67) by solving two equations for these yet two unknowns (we shall not do this explicitly here). As a final step, inverting the Hankel transform leads to the following final expression for the composite moments

[3] That the product of a matrix with a vector on its right is a linear combination of the columns of the matrix is called the 'column point of view of matrix multiplication', see standard modern texts on linear algebra such as Strang (2005) or Lay (2011).

[4] Using the $1/2\pi$ normalization conventions of the Fourier transforms given in Eq. (6.68), the inverse Fourier transform of $1/(k^2+a^2)$ is $e^{-a|z-z'|}/2a$.

$$\begin{aligned}\mathbf{\Phi}(\mathbf{r}) &= \mathbf{\Phi}(\rho, z) \\ &= \frac{h_1}{4\pi}\frac{\mathrm{e}^{-\varsigma_1\sqrt{\rho^2+(z-z')^2}}}{\sqrt{\rho^2+(z-z')^2}}\mathbf{w}_1 - \frac{h_2}{4\pi}\frac{\mathrm{e}^{-\varsigma_2\sqrt{\rho^2+(z-z')^2}}}{\sqrt{\rho^2+(z-z')^2}}\mathbf{w}_2 \\ &\quad + \frac{1}{2\pi}\left(\int_0^\infty c_1(q)\, e^{-\lambda_1(q)z} J_0(qp)\, q\, \mathrm{d}q\right)\mathbf{w}_1 \\ &\quad + \frac{1}{2\pi}\left(\int_0^\infty c_2(q)\, e^{-\lambda_2(q)z} J_0(qp)\, q\, \mathrm{d}q\right)\mathbf{w}_2 \,. \end{aligned} \tag{6.78}$$

Finally, the fluence $\psi_0(z)$ and the reflectance $R(\rho)$ at the boundary $z = 0$ can be calculated for $N = 3$ as

$$\psi_0(z) = \left[\begin{array}{cc} 1 & -2/3 \end{array}\right]\mathbf{\Phi} = \phi_1 - \frac{2}{3}\phi_2 \,, \tag{6.79}$$

$$R(\rho) = \left[\left(\frac{1}{4}+J_0\right),\ -\frac{2}{3}\left(\frac{1}{4}+J_0\right)+\frac{1}{3}\left(\frac{5}{16}+J_2\right)\right]\mathbf{\Phi} + \left[\begin{array}{cc} \dfrac{1+2J_1}{6\mu_1} & \dfrac{J_3}{7\mu_3} \end{array}\right]\frac{\mathrm{d}\mathbf{\Phi}}{\mathrm{d}z} \,. \tag{6.80}$$

These results for the SP_3 equations (derived from the RTE) have been used to compare reflectance values given in Eq. (6.80) with Monte Carlo simulations (Wang and Wu, 2007) and DE solutions (Liemert and Kienle, 2011a). The numerical experiments considered an isotropic point source located at one transport mean free path $l'_{tr} = 1/\mu_1$ inside a semi-infinite homogeneous medium (refractive index 1.4) surrounded by air. For typical values in the near infrared (NIR) ($\mu_a = 0.01\,\mathrm{mm}^{-1}$, $\mu_s = 10\,\mathrm{mm}^{-1}$) and blue or green wavelengths ($\mu_a = 1\,\mathrm{mm}^{-1}$, $\mu_s = 10\,\mathrm{mm}^{-1}$) ranges, the SP_3 equations were shown to give results that better agree with those of Monte Carlo simulations than the DE for distances to the source >1 mm. However, at small distances (<1 mm) to the isotropic point source, the SP_3 displayed no improvements compared to the DE (Liemert and Kienle, 2011a). A comparison of the SP_3 solution (and the DE solution) for an isotropic point source as above with Monte Carlo simulations for an infinitely narrow beam shows that the isotropic solutions do not match well the Monte Carlo results in this case. This means that the approximation of such a beam by an isotropic point source is not a good approximation, contrary to what is pervasively assumed in biomedical optics.

The numerical experiments described in (Liemert and Kienle, 2010; Liemert and Kienle, 2011a) lead naturally to the questions of which order N to employ in a given practical situation, and how accurate it can be near sources. First, searching for an optimal N while exploring higher orders ($N = 5, 7$) should be attempted (Klose and Larsen, 2006). In addition, since the radiative field is more anisotropic near sources, a better accuracy can be achieved with the RTE_d as the starting point to apply the SP_N approximation. Despite these recommendations, there is another problem not covered yet. At short distances to the source, the radiative field is not modified to much extent by scattering and absorption events, and the source emission pattern prevails. In the case of an isotropic point source embedded in the medium, the radiative field propagates along divergent rays starting from the location of the source. Such a situation is not considered by standard radiative transfer models where the divergence of rays always has a cylindrical form (Martí López et al.,

2003). Thus, sources are considered as located at the infinity, presumably a fact inherited from RTT applications in astronomy and astrophysics. Finally, we want to stress that in a comparison with real experimental data, modeling the source is a decisive step, see Ducros (2009) and references therein.

6.3.4 Frequency-domain simplified spherical harmonics equations

Lately, frequency-domain SP_N equations (FD-SP_N) have been derived in biomedical optics (Chu et al., 2009). To obtain the FD-SP_N, as proposed in the literature, the Fourier transform is applied to the time-dependent RTE Eq. (6.1). Hence, the result resembles the time-independent RTE and the previous steps on deriving the SP_N equations Eq. (6.24) are pursued. Finally, the FD-SP_N equations have the same form than that of Eq. (6.24), but with the introduction of the complex-valued nth-order transport coefficients

$$\mu_n^*(\mathbf{r}) = \mu_a(\mathbf{r}) + \frac{i\eta\omega}{c} + \mu_s(\mathbf{r})\left[1 - g_n(\mathbf{r})\right] , \tag{6.81}$$

The FD-SP_N equations and its corresponding BC have thus the same form as Eqs. (6.24) and by considering μ_n^* instead of μ_n and working in the frequency-domain (complex magnitudes). Measurements are then related to the quantization of amplitude, phase and even direct-current exitance (Chu and Dehghani, 2009; Xu et al., 2010; Xu et al., 2011), as it is common in frequency-domain systems (Wang et al., 2008).

A finite element method implementation of the FD-SP_N equations is available in the literature (Chu et al., 2009). In that work, several numerical experiments are performed with a 3-D slab of dimensions $40 \times 20 \times 30\,\mathrm{mm}$. Three different cases are considered (1) an homogeneous medium where $\mu_a = 0.001\,\mathrm{mm}^{-1}$, $\mu_s = 2\,\mathrm{mm}^{-1}$, $g = 0.5$ and $\eta = 1.37$; (2) a similar homogeneous medium with the same optical properties but a different absorption coefficient of $0.01\,\mathrm{mm}^{-1}$ and (3) a three-layer slab where the upper and the bottom sections have identical optical properties of $\mu_a = 0.001\,\mathrm{mm}^{-1}$, $\mu_s = 1\,\mathrm{mm}^{-1}$, $g = 0$ and $\eta = 1.37$. The middle layer has the following optical properties $\mu_a = 0.2\,\mathrm{mm}^{-1}$, $\mu_s = 2\,\mathrm{mm}^{-1}$, $g = 0.5$ and $\eta = 1.37$. A comparison of FD-SP_N-based and DE-based calculations with Monte Carlo simulations demonstrate that for $N > 1$, the FD-SP_N model shows increased accuracy compared with the DE in both the phase and amplitude of boundary data. Also, a high difference was found between the predicted light distribution by the DE and the SP_7 in regions near the source (modeled as an isotropic point source) and regions with high absorption ($0.2\,\mathrm{mm}^{-1}$).

6.3.5 Time-domain simplified spherical harmonics equations

Time-domain SP_N equations (TD-SP_N) have been obtained, implemented and validated to solve problems in radiative transfer and biomedical optics. TD-SP_N models have been derived in three different ways: (*i*) via formal asymptotic analysis (Frank et al., 2007), (*ii*) by direct forward and back-substitution of the moment functions, leading to an integro-differential final form with temporal convolution operators (Bérubé-Lauzière et al., 2009) and (*iii*) imposing diffusive-type conditions

over odd-order moment functions, similarly to the diffusion approximation (Bouza Domínguez and Bérubé-Lauzière, 2010). These three different approaches lead to different equations. The last approach has been to the most studied of the three for problems in biomedical optics. We will thus present the derivation pertaining to the last approach, leading to the so-called the time-dependent parabolic SP_N equations (TD-pSP_N) (Bouza Domínguez and Bérubé-Lauzière, 2010).

For a medium with planar symmetry, the time-dependent RTE only differs from Eq. (6.15) in the additional term $\eta\partial\psi(z,\varpi,t)/c\partial t$. Following the same steps as in Section 6.3.1, we arrive to an expression identical to Eq. (6.20) for the Legendre moments of the radiance, except for the additional term $\eta\partial\psi_n(z,t)/c\partial t$. Now, the direct back substitution of the odd-orders leads to equations with mixed terms of spatial and time partial derivatives. These equations are not of the diffusion-type, but contain convolution operators over the Legendre moment functions (Bérubé-Lauzière et al., 2009). To preserve the parabolic nature of the equations, we impose the following diffusive conditions on the time-derivatives of the odd-order moments (compare with the diffusion approximation Eq. (6.12))

$$\tau_n \left| \frac{\partial}{\partial t}\psi_n(z,t) \right| \ll |\psi_n(z,t)| \,, \quad \tau_n = \frac{\eta l_n}{c} \,. \tag{6.82}$$

These last conditions limit the relative time variation of the odd-order moments within the characteristic time τ_n. For $N = 1$, Eq. (6.82) turns out to be the well-known DA (Eq. (6.12)) for a planar geometry. So far, a complete study of Eq. (6.82) and therefore, the TD-pSP_N model validity, in terms of frequency modulation and pulse width values in time-resolved problems is pending for completion. An analysis of the TD-pSP_N model validity in the solution of forward and inverse problems can influence the design of experimental sets specifically built for using this model.

Imposing the diffusive conditions provides an expression similar to Eq. (6.21). Thus, the algebraic elimination of odd-moments in terms of the even-moments becomes possible. The extension of these results to 3-D and the introduction of the time-dependent vector of composite moments $\mathbf{\Phi}(\mathbf{r},t)$ leads to a system of $K = (N+1)/2$ coupled *parabolic* PDEs. This model, known as the *time-dependent parabolic SP_N equations* (TD-pSP_N) (Bouza Domínguez and Bérubé-Lauzière, 2010), has the same form as Eq. (6.24) except for the introduction of the term $[\eta\partial\mathbf{T}\mathbf{\Phi}(\mathbf{r},t)/c\partial t$. For $N = 1$, TD-pSP_N equations become the DE. Also, in this approach, the boundary conditions remain the same as in the steady-state case.

The TD-pSP_N model has been numerically implemented using a combined finite difference – finite element scheme (Bouza Domínguez and Bérubé-Lauzière, 2010). In this work, the model (for $N = 3$) is compared with DE-based numerical solutions and Monte Carlo simulations. The numerical experiments are carried out in a 2×2 cm homogeneous medium (see Fig. 6.3 left) for two different regimes: (1) a diffusive regime where $\mu_a = 0.04\,\mathrm{cm}^{-1}$, $\mu_\mathrm{s}' = 20\,\mathrm{cm}^{-1}$ and $\eta = 1$ (no refractive index mismatch) and (2) a near-nondiffusive regime (Hielscher et al., 1998) where $\mu_a = 1\,\mathrm{cm}^{-1}$, $\mu_\mathrm{s}' = 10\,\mathrm{cm}^{-1}$ and $\eta = 1$ (also, no refractive index mismatch). An isotropic point source, Dirac delta function in time, is placed at the center of the medium.

In both cases, the time-dependent fluence values are calculated at the boundary using the numerical solution provided by the TD-pSP_3 equations and the DE.

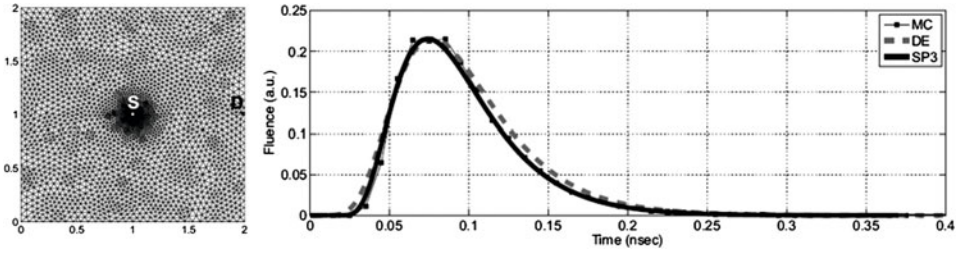

Fig. 6.3. Numerical experiment in a 2-D homogeneous medium (left) with $\eta = 1$, $g = 0.9$ and $\mu_a/\mu_s{}' = 0.1$ (this is a near-nondiffusive regime condition, see Hielscher et al. (1998)) and an isotropic point source, Dirac delta function in time, located at point S. At right, fluence profile at the detector point D calculated using the DE, the TD-pSP_3 equations and the Monte Carlo method. The TD-pSP_3 model better reproduces the Monte Carlo results than the DE, especially for those parts of the curve corresponding to early arriving photons and at long times.

For the diffusive regime, the results showed that TD-pSP_3 equations accurately reproduce the Monte Carlo results. For the near-nondiffusive regime, the TD-pSP_3 solution better reproduces the Monte Carlo results at the early times and at long times than the DE, see Fig. 6.3 at right.

In a second round of experiments, an absorptive inclusion is embedded in a $2 \times 2\,\mathrm{cm}$ homogeneous medium where $\mu_a = 0.01\,\mathrm{cm}^{-1}$, $\mu_s' = 10\,\mathrm{cm}^{-1}$ and $\eta = 1$, see Fig. 6.4. Three increasing values are assumed for the inclusion absorption coefficient $\mu_a = 0.05$, 0.1 and $1\,\mathrm{cm}^{-1}$ (last value corresponding to high absorption). The fluence profile is calculated in the homogeneous medium in the presence and absence of the absorptive inclusion using the TD-pSP_3 equations and the DE. With

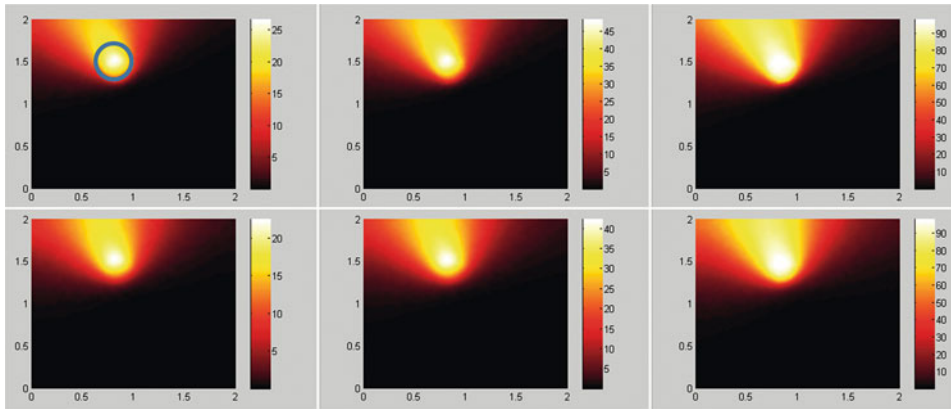

Fig. 6.4. Numerical experiments with a 2-D homogeneous medium ($\eta = 1$, $\mu_a = 0.01\,\mathrm{cm}^{-1}$ and $\mu_s{}' = 10\,\mathrm{cm}^{-1}$) with an isotropic point source (as in Fig. 6.3) and an absorptive inclusion (see small circle in top-left figure) which takes values of 0.05, 0.1 and $1\,\mathrm{cm}^{-1}$ (left to right). Color represents the percentage difference of fluence values with respect to the results in a medium with no inclusion, for the TD-pSP_3 equations (upper row) and the DE (lower row), at 220 ps. The contrast of the fluence fields is higher for the TD-pSP_3 equations than for the DE. This situation is repeated at different times.

these values, the percentage difference of fluence values with respect to the results in a medium with no inclusion is calculated, as a contrast or sensitivity measure, for each model. In all the cases and times, the TD-pSP_3 equations showed a higher sensitivity compared to the DE; see Fig. 6.4. Thus, the TD-pSP_3 equations seem more appropriate for describing light propagation in small geometries in the presence of absorptive inhomogeneities than the DE (Bouza Domínguez and Bérubé-Lauzière, 2010).

6.4 Numerical solutions

In the presence of complex geometries and/or heterogeneous media, it becomes necessary to resort to numerical methods, either implemented on structured or unstructured grids (also called meshes with nodes and elements as components (Jin, 2002)). So far, numerical solutions to SP_N-based equations for boundary problems have been achieved with finite-difference (Klose and Larsen, 2006; Bérubé-Lauzière et al., 2009; Klose and Pöschinger, 2011), finite volume (Montejo et al., 2011) and finite element (Chu et al., 2009; Bouza Domínguez and Bérubé-Lauzière, 2010; Bouza Domínguez and Bérubé-Lauzière, 2011; Lu et al., 2010; Tian et al., 2010; Zhong et al., 2011) methods.

Next, we make a brief exposition of those methods for the solution of SP_N-based equations.

6.4.1 Finite-difference method

Finite difference methods (FDM) rely on structured grids, which confers them several coding advantages as they are less memory demanding (no cell connectivity information is needed) and function values can be identified with grid indices only (Agarwal, 2000). At the cell level, a low function approximation is used, which favors the FDM for regions requiring a large number of cells. On the other hand, complex boundary conditions are difficult to implement by FDM. In addition, representation of irregular (especially curved) geometries by structured grids can be inexact, unless the grid is especially refined at these locations. An alternative in such cases is to use blocking-off region methods or block-structured grids (Talukdar, 2006; Klose and Pöschinger, 2011; Montejo et al., 2010). In the blocking-off method the exterior boundary ∂S is approximated by the junction of grid points lying in S that best approximate ∂S.

To implement the FDM for SP_N—based equations, we consider a regular domain S located in the xy-plane (2-D, for simplicity), enclosed by the curve ∂S. A regular grid composed by $2N_S$ points along the x- and y-axis $\mathbf{r}_i = (x_i, y_i)$ can be defined as

$$x_i = (i-1)\,\Delta x\,, \quad y_i = (j-1)\,\Delta y\,, \quad i,j = 1,\ldots,N_S\,, \tag{6.83}$$

where Δx and Δy are the grid separations along the x- and y-axis, respectively. We order the grid by the values of the i-index first and then by the j-index values. Let the discrete values of each composite moment be denoted by $\overline{\varphi}_{k,i,j} \approx \varphi_k(x_i, y_j)$.

Then, it is convenient to use centered finite difference approximations for the differential operators, see Eq. (6.25), acting over each φ_k as

$$\begin{aligned}-\nabla\cdot(D_k\nabla\varphi_k)\approx\ &-\left(\frac{D_{k,i+1,j}}{\Delta x^2}\right)\overline{\varphi}_{k,i+1,j}\\ &+\left(\frac{D_{k,i+1,j}+D_{k,i-1,j}}{\Delta x^2}+\frac{D_{k,i,j+1}+D_{k,i,j-1}}{\Delta y^2}\right)\overline{\varphi}_{k,i,j}\\ &-\left(\frac{D_{k,i-1,j}}{\Delta x^2}\right)\overline{\varphi}_{k,i-1,j}-\left(\frac{D_{k,i,j+1}}{\Delta y^2}\right)\overline{\varphi}_{k,i,j+1}\\ &-\left(\frac{D_{k,i,j-1}}{\Delta y^2}\right)\overline{\varphi}_{k,i,j-1}\,.\end{aligned}\tag{6.84}$$

With this discrete approximation, the discretized equation for the CW-SP_N model is

$$\begin{aligned}&\left(\overline{\mathbf{K}}+\overline{\mathbf{M}}\right)\overline{\mathbf{\Phi}}_{i,j}=\overline{\mathbf{Q}}_{i,j}\,,\quad \overline{\mathbf{\Phi}}_{i,j}\approx\mathbf{\Phi}\left(x_i,y_j\right)\,,\quad \overline{\mathbf{Q}}_{i,j}\approx\mathbf{Q}\left(x_i,y_j\right)\,,\\ &k=1,\ldots,K\,,\quad i,j=1,\ldots,N_S\,,\end{aligned}\tag{6.85}$$

where the vector $\overline{\mathbf{\Phi}}_{i,j}$ is ordered by the values of the indices i, j and k consecutively. Here, we have introduced the terms $\overline{\mathbf{K}}$ (a diagonal block matrix) and $\overline{\mathbf{M}}$ (block matrix). These matrices are composed themselves of block matrices named $\overline{\mathbf{K}}_k$ and $\overline{\mathbf{M}}_{k_1,k_2}$ which are banded diagonal matrices, respectively. Diagonal entries of $\overline{\mathbf{K}}_k$ and $\overline{\mathbf{M}}_{k_1,k_2}$ have the following form

$$\begin{aligned}&\mathrm{diag}_{(0)}\left(\overline{\mathbf{K}}_k\right)(i,j)=\frac{D_{k,i+1,j}+D_{k,i-1,j}}{\Delta x^2}+\frac{D_{k,i,j+1}+D_{k,i,j-1}}{\Delta y^2}\,,\\ &\mathrm{diag}_{(1)}\left(\overline{\mathbf{K}}_k\right)(i,j)=-\frac{D_{k,i+1,j}}{\Delta x^2}\,,\\ &\mathrm{diag}_{(-1)}\left(\overline{\mathbf{K}}_k\right)(i,j)=-\frac{D_{k,i-1,j}}{\Delta x^2}\,,\\ &\mathrm{diag}_{(N_s-1)}\left(\overline{\mathbf{K}}_k\right)(i,j)=-\frac{D_{k,i,j+1}}{\Delta y^2}\,,\\ &\mathrm{diag}_{-(N_s-1)}\left(\overline{\mathbf{K}}_k\right)(i,j)=-\frac{D_{k,i,j-1}}{\Delta y^2}\,,\end{aligned}\tag{6.86}$$

$$\mathrm{diag}_{(0)}\left(\overline{\mathbf{M}}_{k_1,k_2}\right)=\mathbf{C}\left(k_1,k_2\right)\big|_{i,j}\,,\quad k_1,k_2=1,\ldots K\,,\tag{6.87}$$

where $\mathbf{C}\left(k_1,k_2\right)\big|_{i,j}$ means that we evaluate at the grid indices (i,j) the entry (k_1,k_2) of the matrix $\mathbf{C}$, see Eq. (6.26). For the FD-SP_N model, we obtain a similar system to Eq. (6.85), but with the complex nth order transport coefficients (Eq. (6.81)) in the matrix entries of Eqs. (6.86) and (6.87).

To derive a discrete formulation for the time-dependent parabolic SP_N equations, the time derivative can be replaced by a finite difference scheme. For this, the total time of study T is divided in regular intervals of size Δt and samples t_m for the time variable are generated as

$$t_m=m\Delta t\,,\quad \Delta t=\frac{T}{M}\,,\quad m=0,\ldots,M-1\,.\tag{6.88}$$

Implicit finite difference schemes, such as the forward Euler or the Crank–Nicholson (CN) schemes (Agarwal, 2000), are preferred to insure unconditional stability. Introducing a control parameter $\theta \in [0,1]$, the different difference schemes for the time-dependence can be written in a unified way as

$$\left(\frac{\eta}{c\Delta t}\overline{\mathbf{T}}+\theta\overline{\mathbf{K}}+\theta\overline{\mathbf{M}}\right)\overline{\mathbf{\Phi}}_{i,j}^{m+1} = \left[(1-\theta)\overline{\mathbf{K}}+(1-\theta)\overline{\mathbf{M}}\right]\overline{\mathbf{\Phi}}_{i,j}^{m}+\theta\overline{\mathbf{Q}}_{i,j}^{m+1}+(1-\theta)\overline{\mathbf{Q}}_{i,j}^{m}, \tag{6.89}$$

where the matrix $\overline{\mathbf{T}}$ has the same type of structure as $\overline{\mathbf{M}}$. The value $\theta = 0$ corresponds to the explicit or backward scheme (conditionally stable), $\theta = 1/2$ is the Crank–Nicholson scheme, and $\theta = 1$ is the full implicit scheme, with the latter two being unconditionally stable.

Solving Eqs. (6.85) and (6.89) leads to high-dimensional sparse linear systems, which means that sparse matrix techniques can be used to save storage requirements, and solutions can be calculated in highly reduced CPU times compared to dense matrix techniques (Saad, 2003). Moreover, direct and iterative methods for solving sparse linear systems are widely available in the literature (Saad, 2003; Davis, 2006; Press et al., 2007).

6.4.2 Finite volume method

The finite volume method (FVM) is a *conservative* discretization method (Versteeg and Malalasekera, 2007). The partial differential equations serving as forward model are transformed into an integral formulation of the underlying conservation laws and discretized directly in physical space. The physical volume V is partitioned into small volumes ΔV called 'cells', with such a partition to be denoted by τ here. The partition τ can be carried in the form of regular or irregular meshes, e.g. a distribution of cubes or a mesh of tetrahedrae (Versteeg and Malalasekera, 2007). The magnitudes of interest in the problem to which the FVM is applied are replaced in the equations by their average values in 'cells'. This step is carried out after integrating the equations over the partition τ. A cell-centered scheme stores the variable values at all cell centers whereas a node-centered scheme stores the variable values at the nodes. The FVM allows the discrete representation of complex volumes without the implicit FDM implementation mesh refinement on irregular boundaries. Furthermore, cell averaging diminishes the problem dimensionality (number of unknowns) which is convenient for large volumes. As a disadvantage, the FVM does not provide accurate results in the case of discontinuous (or widely varying) coefficients that can appear in the forward model. This problem can be avoided if the coefficient discontinuities coincide with cell boundaries, which can be achieved by refining the mesh (at the cost of increasing the problem dimensionality).

To apply the FVM to SP_N—based equations, we make a partition τ of the volume of interest V into non-overlapping control volumes ΔV_i centered at the mesh points p_i. Next, we follow the node-centered scheme as presented in (Montejo et al., 2011) for the CW-SP_N model. The integration of Eqs. (6.24) over a finite volume ΔV centered at the mesh point p yields

$$-\iint_{\partial\Delta V}\overline{D}\nabla\mathbf{\Phi}\cdot\hat{\mathbf{n}}\,\mathrm{d}S+[\mathbf{C}]_p[\mathbf{\Phi}]_p\Delta V=[\mathbf{Q}]_p\Delta V\,, \tag{6.90}$$

where the Gauss–Ostrogradsky Theorem has been applied to obtain the first term, and where $\mathrm{diag}_{(0)}\left(\overline{D}\right) = [D_1 \quad D_2 \quad \cdots \quad D_K]$, $k = 1, \ldots, K$ (this term can be approximated by its value at p), $\partial\Delta V$ denotes the boundary of ΔV composed of a number of faces, $\hat{\mathbf{n}}_{\partial\Delta V}$ is the outer normal to $\partial\Delta V$, and the notation $[\,]_p$ represents the discrete approximation of the enclosed magnitude at the center p of a finite volume element. The vector $[\mathbf{\Phi}]_p$ is ordered by each mesh node p and by the k index, consecutively, i.e. the values for φ_1 for all the nodes come first, then followed by the values of φ_2, etc.

The first term of Eq. (6.90), i.e.

$$J^{(\mathbf{\Phi})}_{n,\Delta V} = -\iint\limits_{\partial\Delta V} \overline{D}\nabla\mathbf{\Phi}\cdot\hat{\mathbf{n}}_{\partial\Delta V}\,\mathrm{d}S\,, \tag{6.91}$$

represents a flux through $\partial\Delta V$. Eq. (6.91) can be approximated by replacing the gradient operation with finite differences at each face composing $\partial\Delta V$. If such approximations are used for the flux term for all control volumes (including boundary conditions in the same way), Eq. (6.90) generates the following matrix system

$$\left\{\widehat{\mathbf{K}} + [\mathbf{C}]_p\right\}[\mathbf{\Phi}]_p = [\mathbf{Q}]_p\,, \tag{6.92}$$

where $\widehat{\mathbf{K}}$ is a $K \times K$ block *diagonal matrix* composed of A_k sparse banded matrices whose explicit form depends on the chosen finite difference scheme at the faces. Eq. (6.92) is a linear system whose solution can be obtained by the GMRES or matrix decomposition (if it is advantageous, given the problem dimensionality) methods (Press et al., 2007).

For the FD-SP_N model, the resulting equation will have the same form as Eq. (6.92), except for considering the complex nth-order transport coefficients (see Eq. (6.81)) in the matrix entries. For the time-dependent parabolic SP_N equations we obtain a system of differential equations

$$\left\{\widehat{\mathbf{K}} + [\mathbf{C}_p + \frac{\eta}{c}\frac{\mathrm{d}}{\mathrm{d}t}[\mathbf{T}]_p\right\}[\mathbf{\Phi}(t)]_p = [\mathbf{q}]_p\,, \tag{6.93}$$

which again can be solved using finite differences with a control parameter $\theta \in [0, 1]$, (compare with Eq. (6.89)

$$\begin{aligned}\left(\frac{\eta}{c\Delta t}[\mathbf{T}]_p + \theta\widehat{\mathbf{K}} + \theta[\mathbf{C}]_p\right)[\mathbf{\Phi}]_p^{m+1} \\ = \left[(1-\theta)\widehat{\mathbf{K}} + (1-\theta)[\mathbf{C}]_p\right][\mathbf{\Phi}]_p^m + \theta[\mathbf{Q}]_p^{m+1} + (1-\theta)[\mathbf{Q}]_p^m\,.\end{aligned} \tag{6.94}$$

The structure of Eq. (6.94) suggests the use of matrix decomposition methods to accelerate the iterative process of finding the solution. Otherwise, the generalized minimal residual method (GMRES) can be employed. Alternatively for the time variable, Runge–Kutta techniques can be used.

6.4.3 Finite element method

The finite element method (FEM) is a highly versatile approach for dealing with media with intricate geometries and heterogeneous distributions of material (here optical) properties (Jin, 2002). Boundary conditions are added to the formulation naturally, no matter the boundarie's complexity. As with the FVM, the FEM starts with a partition of the volume of interest into non-overlapping elements. The information on the partition or mesh takes the form of nodes and elements that are related by a connectivity matrix. In the FEM, functions representing optical properties or the light profile in the medium are approximated by piecewise linear functions or polynomials within each element. Hence, a highly refined mesh is not needed in regions with spatially slowly varying functions. Compared with the FVM, the FEM is usually more computationally intensive in terms of the problem dimensionality. The FEM exclusively deals with functions evaluated at nodes, while in the FVM it is possible to only deal with point-averaged information.

To implement the FEM for the CW-SP_N model, the volume of interest is partitioned into l non-overlapping elements τ_j, $j = 1, \ldots, l$, such that $V = \bigcup_{j=1}^{l} \tau_j$. The elements are defined via d vertex nodes $\widetilde{\mathbf{N}}_i$, $i = 1, \ldots, d$. The nodes can be separated into d_1 internal nodes and d_2 boundary nodes where the boundary conditions are satisfied. Thus, $d = d_1 + d_2$ and the solution $\mathbf{\Phi}(\mathbf{r})$ to Eq. (6.24) can be approximated by the piecewise polynomial and continuous function $\mathbf{\Phi}^h(\mathbf{r})$ as

$$\mathbf{\Phi}(\mathbf{r}) \approx \mathbf{\Phi}^h(\mathbf{r}) = \sum_{i=1}^{d} \mathbf{\Phi}_i u_i(\mathbf{r}) \,, \quad u_i(\mathbf{r}) \in \Omega^h \,, \tag{6.95}$$

where Ω^h is a finite-dimensional subspace spanned by the basis functions $u_i(\mathbf{r})$, $i = 1, \ldots, d$. Hence, we can find $\widetilde{\mathbf{\Phi}} = \{\mathbf{\Phi}_i\}$, $i = 1, \ldots, d$ from which the solution can be obtained everywhere through the interpolation rule given in Eq. (6.95). Using the Galerkin method (Jin, 2002; Gockenbach, 2006), we can calculate the equivalent numerical solution of Eq. (6.24) $\widetilde{\mathbf{\Phi}}$ as

$$\left[\widetilde{\mathbf{K}} + \widetilde{\mathbf{M}} + \widetilde{\mathbf{\Pi}}\right] \widetilde{\mathbf{\Phi}} = \widetilde{\mathbf{F}} + \widetilde{\mathbf{\Gamma}} \,. \tag{6.96}$$

Here, $\widetilde{\mathbf{K}}$ represents a 'compound' stiffness matrix and can be described as a diagonal block matrix composed of 'elemental stiffness matrices' $\widetilde{\mathbf{K}}_k$, $k = 1, \ldots, K$, with entries (i, j) given by the expressions

$$\widetilde{\mathbf{K}}_k\,(i,j) = \int_V \frac{1}{(4k-1)\,\mu_{2k-1}} \nabla u_i(\mathbf{r}) \cdot \nabla u_j(\mathbf{r}) \mathrm{dV} \,, \quad k = 1, \ldots, K \,, \quad i, j = 1, \ldots, d \,. \tag{6.97}$$

The structure of the 'compound' mass matrix $\widetilde{\mathbf{M}}$ is similar to the matrix $\overline{\mathbf{M}}$ discussed for the FDM method and it is composed of 'elemental mass matrices' $\widetilde{\mathbf{M}}_{k_1,k_2}$, $k_1, k_2 = 1, \ldots, K$ with the following entries

$$\widetilde{\mathbf{M}}_{k_1,k_2}\,(i,j) = \int_V C\,(k_1,k_2)\, u_i(\mathbf{r}) u_j(\mathbf{r}) \mathrm{dV} \,, \quad k_1, k_2 = 1, \ldots, K \,, \quad i, j = 1, \ldots, d \,, \tag{6.98}$$

where $\mathrm{C}(k_1, k_2)$ are the elements of the matrix $\mathbf{C}$ (Eq. (6.26)). The structure of matrix $\widetilde{\mathbf{\Pi}}$ is also similar to $\overline{\mathbf{M}}$ and it is composed of matrices $\widetilde{\mathbf{\Pi}}_{k_1,k_2}$, $k_1, k_2 = 1, \ldots, K$, with the following entries

$$\widetilde{\mathbf{\Pi}}_{k_1,k_2}(i,j) = \int_{\partial V} \frac{\Theta(k_1,k_2)}{(4k_1-1)\,\mu_{2k_1-1}} u_i(\mathbf{r}) u_j(\mathbf{r})\,\mathrm{d}\sigma\,,$$
$$k_1, k_2 = 1, \ldots, K\,, \quad i,j = 1, \ldots, d \tag{6.99}$$

where $\mathrm{d}\sigma$ is an element of area on the boundary ∂V and $\Theta(k_1, k_2)$ are the elements of the matrix $\mathbf{\Theta} = \mathbf{B}^{-1}\mathbf{A}$, see the boundary matrices $\mathbf{A}$ and $\mathbf{B}$ in Eq. (6.28).

The 'compound' force load vector $\widetilde{\mathbf{F}}$ is composed of terms $\widetilde{\mathbf{F}}_k$, $k = 1, \ldots, K$, ('elemental force load vectors') which are column vectors with the following entries

$$\widetilde{\mathbf{F}}_k = \int_V Q(k) u_i(\mathbf{r})\mathrm{dV}\,, \quad k = 1, \ldots, K\,, \quad i = 1, \ldots, d\,, \tag{6.100}$$

where $Q(k)$ are the components of column vector $\mathbf{Q}$.

The column vector $\widetilde{\mathbf{\Gamma}}$ is similar to $\widetilde{\mathbf{F}}$ and originates from the external source distribution $\mathbf{S}$ at the boundary. This vector is composed of terms $\widetilde{\mathbf{\Gamma}}_k$, $k = 1, \ldots, K$, which are column vectors of length d_1 given by

$$\widetilde{\mathbf{\Gamma}}_k(i) = \int_{\partial V} \frac{G(k)}{(4k-1)\,\mu_{2k-1}} u_i(\mathbf{r}) u_j(\mathbf{r})\,\mathrm{d}\sigma\,, \quad k = 1, \ldots, K\,, \quad i = 1, \ldots, d\,, \tag{6.101}$$

where $G(k)$ are the elements of the vector $\mathbf{G} = \mathbf{B}^{-1}\mathbf{S}$.

As for the previous numerical methods discussed, the discretized equations for the FD-SP_N model have the same form as for the steady-state situation, but substituting the transport coefficient by the complex transport coefficients (Eq. (6.81)). For the TD-pSP_N equations, we can write directly the FEM-discretized equations as

$$\left[\widetilde{\mathbf{K}} + \widetilde{\mathbf{M}} + \widetilde{\mathbf{\Pi}} + \frac{\eta\widetilde{\mathbf{T}}}{c}\frac{\mathrm{d}}{\mathrm{d}t}\right]\widetilde{\mathbf{\Phi}}(t) = \widetilde{\mathbf{F}} + \widetilde{\mathbf{\Gamma}}\,, \tag{6.102}$$

where the matrix $\widetilde{\mathbf{T}}$ has an expression similar to that of $\widetilde{\mathbf{M}}$, with analogous entries

$$\widetilde{\mathbf{T}}_{k_1,k_2}(i,j) = \int_V T(k_1,k_2)\, u_i(\mathbf{r}) u_j(\mathbf{r})\mathrm{dV}\,, \quad k_1, k_2 = 1, \ldots, K\,, \quad i,j = 1, \ldots, d\,, \tag{6.103}$$

The solution of Eq. (6.102) can be achieved by a finite difference scheme or Runge–Kutta methods as previously for the FDM and FVM approaches (Eqs. (6.89) and (6.94)).

6.5 Diffuse optical tomography based on SP_N models

Diffuse optical tomography is an imaging technique that aims to recover interior maps based on the transillumination of a biological body and the (generally exterior) measurement of the light that has propagated through the body. DOT involves the recording of the exiting light and digital data processing, to obtain representative images of the relevant internal properties of the biological body (Wang and Wu, 2007). Model-based iterative image reconstruction algorithms in DOT rely on the accuracy of a discretized forward model to reproduce collected measurements (Klose and Hielscher, 2008; Dehghani et al., 2009; Arridge and Schotland, 2009). Lately, model-based DOT has been attempted with the FD-SP_N (Chu and Dehghani, 2009) and the TD-pSP_N equations (Bouza Domínguez and Bérubé-Lauzière, 2011b; Bouza Domínguez and Bérubé-Lauzière, 2011c). We now proceed to describe the main features and results of the implemented DOT algorithms with these models.

6.5.1 DOT based on the FD-SP_N model

For the FEM-discretized FD-SP_N model, the inverse problem has been posed as an unconstrained optimization problem with a regularization term (Chu and Dehghani, 2009; Wang et al., 2011)

$$\boldsymbol{\mu} = \underset{\{\boldsymbol{\mu}^h\}}{\operatorname{argmin}} \sum_{s=1}^{S} \sum_{d=1}^{D} \left(M_{s,d} - P_{s,d}\right)^2 + \lambda \left(\boldsymbol{\mu}^h - \boldsymbol{\mu}_0\right)^2, \tag{6.104}$$

where 'argmin' stands for argument of the minimum. In the last equation, the vector $\boldsymbol{\mu}$ represents the nodal values of an optical parameter set (e.g. absorption and scattering coefficients); the summation is over the total number of configuration sources S (modeled as isotropic point sources) and detector positions D, and the terms $M_{s,d}$ and $P_{s,d}$ represent the measurements and the forward model predictions, respectively. Phase and amplitude data are considered in Eq. (6.104). The Tikhonov regularization parameter λ appears multiplying the L_2-regularization term, where $\boldsymbol{\mu}_0$ represents the *a priori* estimate of $\boldsymbol{\mu}$. The solution to the optimization problem cast in Eq. (6.104) is found by the Levenberg–Marquardt method (Press et al., 2007) which employs Jacobian calculations of phase and amplitude with respect to $\boldsymbol{\mu}$. The Jacobian calculations are performed using the perturbation method and the reciprocity approach, see (Arridge and Schotland, 2009) for details.

In (Chu and Dehghani, 2009), several numerical experiments are conceived to test the FD-SP_N model performance on retrieving the absorption and scatter properties. The experiments involve small geometries and tissue typical optical coefficient values in the NIR spectrum, see the article for details. A distinction in the retrieved image accuracy, artefact presence (significant near the boundary) and cross-talk effects is found for different orders N. Particularly, for $N = 3$ and 5 the reconstructions performed acceptably well. Errors in the reconstructed values are within 24% of the expected values and the worse results are obtained by the DE (SP_1) in the absorption coefficient reconstruction. The reported results support the use of the FD-SP_N model (orders $N = 3$ and 5) in DOT. The authors explained that further improvements in the image reconstructions can be expected with the optimization of the regularization parameter and selection of stopping criteria.

6.5.2 DOT based on the TD-pSP_N model

Recently, DOT based on the FDM-FEM discretized TD-pSP_N equations has been carried out (Bouza Domínguez and Bérubé-Lauzière, 2011b; Bouza Domínguez and Bérubé-Lauzière, 2011c). This time, the inverse problem is posed as the following constrained optimization problem

$$\boldsymbol{\mu} = \underset{\{\boldsymbol{\mu}^h\}}{\operatorname{argmin}} \frac{1}{2} \sum_{s=1}^{S} \sum_{d=1}^{D} \sum_{m=1}^{M} \left(\frac{M_{s,d}^{(m)} - P_{s,d}^{(m)}}{\sigma_{s,d}} \right)^2 , \quad P_{s,d}^{(m)} = \widehat{M} \widetilde{\boldsymbol{\Phi}}_s^{(m)}$$
$$\text{subject to} \begin{cases} \widetilde{\mathbf{W}} \widetilde{\boldsymbol{\Phi}}_s^{(m)} = \left(\frac{\eta}{c}\right) \widetilde{\mathbf{T}} \widetilde{\boldsymbol{\Phi}}_s^{(m-1)} + \widetilde{\boldsymbol{\Upsilon}}_s^{(m)} , \quad m = 1, \ldots, M , \quad s = 1, \ldots, S \\ \boldsymbol{\mu}_l \leq \boldsymbol{\mu} \leq \boldsymbol{\mu}_u , \end{cases} , \tag{6.105}$$

The same notation as in Eq. (6.104) is used. An additional summation over the time steps appears here in the objective function compared to that in Eq. (6.104) to account for the time dependence of the light field. The quantities $\sigma_{s,d}^{(m)}$ are the standard deviations of the measurements; which are mainly determined by shot noise. $\widehat{M}$ is the measurement operator which acts over the time-dependent vector of composite moments $\widetilde{\boldsymbol{\Phi}}_s^{(m)}$. The matrix $\widetilde{\mathbf{W}} = \Delta t\big(\widetilde{\mathbf{K}} + \widetilde{\mathbf{M}} + \widetilde{\boldsymbol{\Pi}}\big) + (\eta/c)\widetilde{\mathbf{T}}$ and vector $\widetilde{\boldsymbol{\Upsilon}}^{(m)} = \Delta t\big[\widetilde{\mathbf{F}}^{(m)} + \widetilde{\boldsymbol{\Gamma}}^{(m)}\big]$ result from the FDM-FEM numerical discretization scheme; see Section 6.4 (the Euler finite difference scheme is employed). The vectors $\boldsymbol{\mu}_l$ and $\boldsymbol{\mu}_u$ are lower and upper bounds over the set of optical coefficients $\boldsymbol{\mu}$ to be recovered.

The inverse problem cast in Eq. (6.105) contains the forward model and bounds over the optical coefficient values as constraints. In addition, the time-dependence of the forward model increases the complexity of the optimization problem mainly because of the necessary time-stepping and the increased dimensionality of the problem compared to the CW and FD cases. In (Bouza Domínguez and Bérubé-Lauzière, 2011b; Bouza Domínguez and Bérubé-Lauzière, 2011c), the authors decided to employ a 'nested analysis and design' (NAND) method (Hazra, 2010). Basically, in the NAND method the implicit dependence of the state constraints (or $\widetilde{\boldsymbol{\Phi}}_s^{(m)}$; we employ terminology of constrained optimization theory) with the design variables (or $\boldsymbol{\mu}$) is considered. Then, constraints posed by the forward model are eliminated. The solution to the optimization problem given in Eq. (6.105) is obtained through a Sequential Quadratic Programming (SQP) algorithm (Nocedal, and Wright, 2006). SQP uses the gradient of the objective function in the iteration process and a Hessian approximation by the damped BFGS method to avoid computing second derivatives. Finally, a time-dependent adjoint differentiation scheme (see Arridge and Schotland (2009) for the topic of adjoint variables) is utilized to calculate the gradient and reduce the computation time.

To investigate the performance of the TD-pSP_N model in recovering optical properties of biological media, several numerical experiments are conducted in (Bouza Domínguez and Bérubé-Lauzière, 2011b; Bouza Domínguez and Bérubé-Lauzière, 2011c). The experiments involve a circular two-dimensional medium (background medium) with a 1.5 cm of radius. The medium is homogeneous with

optical properties $\mu_a = 0.01\,\mathrm{cm}^{-1}$, $\mu_s = 80\,\mathrm{cm}^{-1}$, $g = 0.9$ and $\eta = 1.4$ and it is considered as surrounded by air. In the multi-parameter reconstructions, absorptive and scattering inclusions are embedded in the background medium; see Fig. 6.5. Increasing values of μ_a for the absorptive inclusion are considered: 0.05, 0.1, and $1\,\mathrm{cm}^{-1}$ (high-absorption case) which correspond to diffusion coefficient values of 0.0414, 0.0412 and 0.037 cm. For the scattering inclusion, the value of $120\,\mathrm{cm}^{-1}$ is assumed for its scattering coefficient. Multi-parameter reconstructions (absorption and diffusion coefficient maps) were performed with the DE and the TD-pSP_N equations as the forward models and the results compared, see (Bouza Domínguez and Bérubé-Lauzière, 2011b; Bouza Domínguez and Bérubé-Lauzière, 2011c) for details.

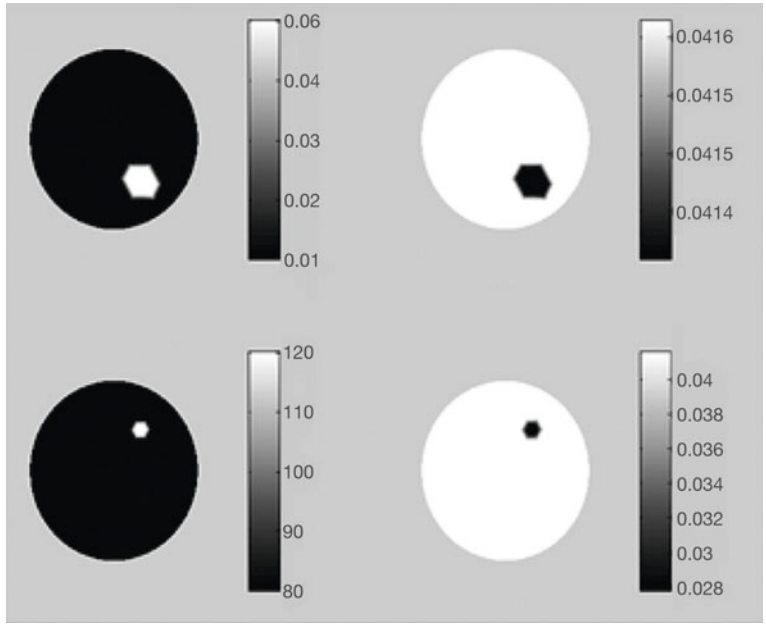

Fig. 6.5. Numerical experiments for the multi-parametric inverse problem. Absorption (only one value of $\mu_a = 0.05\,\mathrm{cm}^{-1}$ is represented) and scattering coefficient ($120\,\mathrm{cm}^{-1}$) distribution (top and bottom, left column) and diffusion coefficient distribution for each type of inclusion (top and bottom, right column).

In all the experiments, the TD-pSP_N model ($N > 1$) recovered accurately the absorptive and scattering inclusion values; see Bouza Domínguez and Bérubé-Lauzière (2011b) and Bouza Domínguez and Bérubé-Lauzière (2011c) for the comparison details. Particularly, the results obtained with $N = 3$ outperformed the DE. For the reconstructed absorption maps, the errors with respect to the original values (in percent, taking the maximum of the reconstructed values) for the DE are of 19%, 16% and 8% ($\mu_a = 0.05$, 0.1, and $1\,\mathrm{cm}^{-1}$). The corresponding errors for the TD-pSP_3 equations are of 0.1%, 8% and below 1%; see Figs. 6.6 and 6.7 and compare with Fig. 6.5, to partly appreciate these results. For the reconstructed dif-

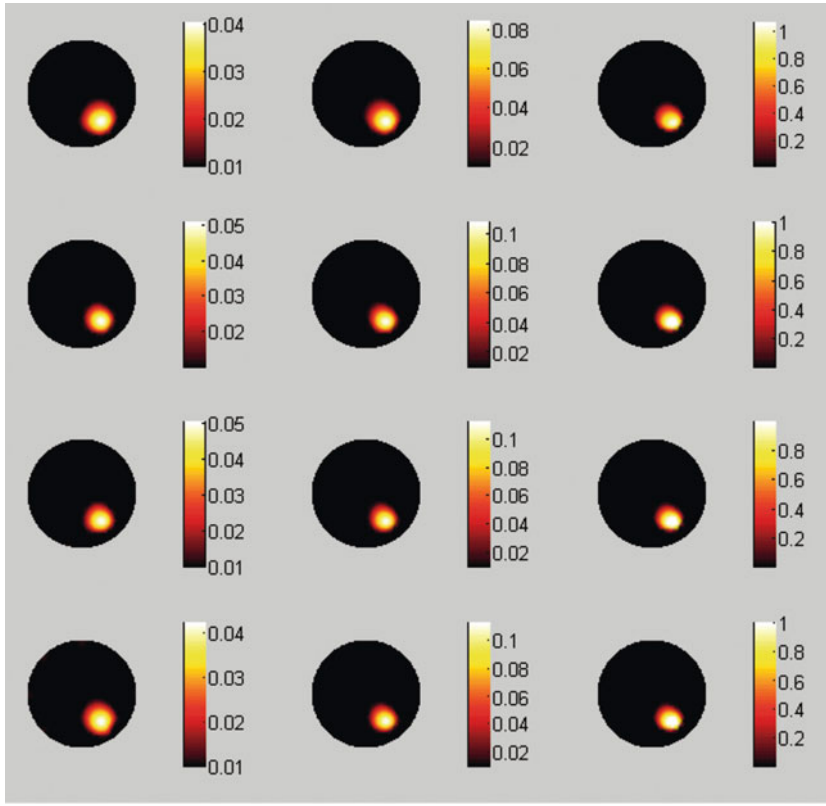

Fig. 6.6. Solution of the inverse problem (absorption coefficient map) for the multi-parametric inverse problem. The background (circle) optical properties are $\mu_a = 0.01\,\mathrm{cm}^{-1}$, $\mu_s = 80\,\mathrm{cm}^{-1}$, $g = 0.9$ and $\eta = 1.4$ and the medium is considered as surrounded by air. Values of the absorption coefficient for the absorptive inclusion are: 0.05, 0.1, and $1\,\mathrm{cm}^{-1}$ (left to right). Images are plotted for the orders $N = 1$, 3, 5 and 7 (first, second, third and fourth rows).

fusion maps, the DE and the TD-pSP_3 equations presented approximately the same errors in the reconstruction of the scattering heterogeneity in the cases $\mu_a = 0.05$ and $0.1\,\mathrm{cm}^{-1}$. For the case $\mu_a = 1\,\mathrm{cm}^{-1}$, the DE error is greater than 40% while in the case of the TD-pSP_3 equations it is only 6%. A similar behaviour is observed for the same reconstructed diffusion maps but at the position of the absorptive inclusion. In addition, reconstructed images presented artifacts (almost negligible spots, at the boundary) and cross-talk effects which vary with the order N, with the DE-based reconstructions delivering the worst results. In this work, the authors concluded that the DOT algorithm based on the TD-pSP_N model ($N > 1$) can accurately replace DE-based algorithms, especially in the physical situations where the DE fails.

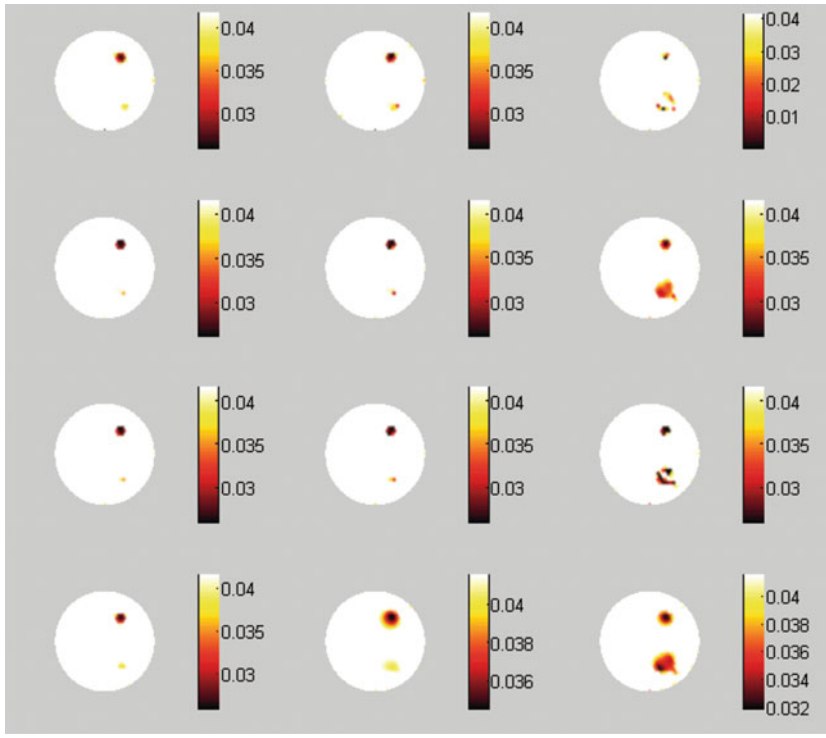

Fig. 6.7. Solution of the inverse problem (diffusion coefficient map) for the multi-parametric inverse problem. The background (circle) optical properties are $\mu_a = 0.01\,\mathrm{cm}^{-1}$, $\mu_s = 80\,\mathrm{cm}^{-1}$, $g = 0.9$ and $\eta = 1.4$ and the medium is considered as surrounded by air. Images are plotted for the orders $N = 1$, 3, 5 and 7 (first, second, third and fourth rows) where the absorptive heterogeneity takes the following values: 0.05, 0.1, and $1\,\mathrm{cm}^{-1}$ (left to right). At the absorptive heterogeneity (see Fig. 6.5), the diffusion coefficient takes the following values $D = 0.0414$, 0.0412 and 0.037 cm. At the scattering heterogeneity (see Fig. 6.5), the diffusion coefficient has the value $D = 0.0277\,\mathrm{cm}$.

6.6 Molecular imaging of luminescence sources based on SP_N models

Optical molecular imaging of luminescence sources (OMI) is a promising discipline of biomedical optics. OMI allows the study of biological processes and medical treatment, as well as the diagnosis and follow-up of diseases (Weissleder and Ntziachristos, 2003; Hielscher, 2005; Ntziachristos, 2006; Rao et al., 2007; Willmann et al., 2008; Klose, 2009; Mitchell et al., 2011; Elwell and Cooper, 2011). Compared to intrinsic imaging (or DOT), luminescent light increases measurement sensitivity of experimental systems to specific targets or physiological processes occurring in biological tissues (Weissleder and Ntziachristos, 2003; Hielscher, 2005; Ntziachristos, 2006). Applications of OMI are mainly focused in small animal imaging, although clinical imaging has been lately targeted (Burgess et al., 2010; Pleijhuis et al., 2011). Tomographic methods in OMI would supply researchers and physicians with

three-dimensional visualization of tissue structure and functions. Current modalities are bioluminescence and fluorescence imaging and, more recently, Cerenkov luminescence imaging (Mitchell et al., 2011). Tomographic imaging by these methods involves the solution of an inverse source problem. For solving an inverse source problem, the optical properties of the medium are needed. Optical properties of luminescence emitting media (or substrate media) can be supplemented by additional anatomical information from CT/MRI scans and tabulated optical coefficient values (Alexandrakis et al., 2005; Alexandrakis et al., 2006; Klose et al., 2010). If no *a priori* information exists about the substrate medium, or the information is insufficient, a complementary DOT reconstruction can be carried.

Inverse problems based on deterministic models frequently use the DE (Naser and Patterson, 2011; Larusson et al., 2011; Zhu et al., 2011). However, in many practical situations luminescence sources are located deep into small geometries of tissue, in the presence of high absorption, such as of internal organs. Under those conditions, the DE fails as a model of light propagation in tissues and transport calculations are mandatory to gain in accuracy (Hielscher et al., 1998). In this context, deterministic models based on the SP_N approximation are preferred and used to perform OMI. In this section, we review recent results on the use of SP_N-based models in bioluminescence and fluorescence DOT. We also include the latest applications of SP_N-based models in Cerenkov optical imaging.

6.6.1 Bioluminescence imaging

Bioluminescence originates in chemical reactions and does not require external excitation sources (Klose, 2009; Contag and Bachmann, 2002; Welsh and Kay, 2005; Vo-Dinh, 2003). The chemical reactions involve the interaction of an administered light-producing substrate (usually luciferine) and a transfected enzyme (luciferase from firefly, Renilla, or Aequorin). Luciferase catalyzes the oxidation of luciferine. causing light emission. The bioluminescent source density changes slowly with time and the source can be assumed to be steady. Although the DE is frequently used as the forward model, at emission wavelengths less than <650 nm (Renilla or Gaussia luciferase) light is strongly absorbed by tissues, violating the limits of DE validity. In addition, the ratio μ_s'/μ_a at visible and NIR wavelengths varies over a wide range for some organs such as bone, and for others such as heart and liver, this ratio does not go beyond 10 (Vo-Dinh, 2003). Hence, physical situations where transport calculations are necessary can occur (Hielscher et al., 1998). These difficulties are aggravated in the presence of small geometries and isotropic point-like bioluminescence sources, circumstances where the DE is out of its comfort zone (Martí López et al., 2004; Hielscher et al., 1998; Klose and Larsen, 2006).

To overcome the drawbacks of the DE in such situations, the CW-SP_N model (Eq. (6.24)) has been used as the forward model in bioluminescence imaging (Klose et al., 2010; Lu et al., 2009; Tian et al., 2010; Klose, 2012). Particularly, the CW-SP_3 equations are frequently chosen, since they can provide transport-like solutions with low computational cost (Klose et al., 2010). Reconstruction techniques with the CW-SP_3 equations also employ spectrally resolved information in order to reduce the inherent ill-posedness of inverse source problems (Lu et al., 2009). In the literature, the following reconstruction techniques for small animal imaging have

been attempted: (*i*) a gradient-based optimization method with regularization (Lu et al., 2009), (*ii*) the algebraic reconstruction method, with *a priori* estimation of the absorption distribution by an evolution strategy (ES) algorithm (Klose et al., 2010) and a generalized graph cuts optimization method (Tian et al., 2010). Next, we provide some details on the mentioned source reconstruction techniques.

In (Lu et al., 2009), a FEM discretization of the CW-SP_3 equations is used to calculate the model predictions as the exitance values $J_{no}^{(out)}$. Then, the following bound-constrained least-squares problem is posed

$$\min_{\mathbf{0}<\mathbf{Q}<\mathbf{Q}^{\sup}} \left\|\mathbf{A}_{(FEM)}\mathbf{Q}-\mathbf{M}\right\| + \lambda\eta(\mathbf{Q})\,, \tag{6.106}$$

where $\|\ \|$ represents the L_2 or Euclidean norm, $\mathbf{Q}^{sup}$ is the upper bound of the source density distribution $\mathbf{Q}$, the matrix $\mathbf{A}_{(FEM)}$ appears in the FEM discretization process and includes the measurement operator $\widehat{M}$ (see Eqs. (6.33) and (6.96)), $\mathbf{M}$ is the vector of measurements, λ is the regularization parameter and $\eta(\mathbf{Q})$ is a penalty function. The minimization of Eq. (6.106) is performed by the limited memory variable metric-bound constrained quasi-Newton method (BLMVM) (Benson and Moré, 2001). In the BLMVM, an approximate Hessian is calculated by vector-vector multiplications, which assures easy matrix inversion and reduces memory and computation time. An implementation of the BLMVM is available in the Toolkit for Advance Optimization (TAO) (Website TAO, 2012). A fully parallel version of the reconstruction algorithm including FEM assembly is also provided in (Lu et al., 2009).

In Klose et al. (2010), an ES algorithm minimizes an objective function similar to Eq. (6.106) (no regularization term is included this time) to estimate the average absorption coefficients at each wavelength. The goal is to diminish the inaccuracy on the determination of the optical parameters which could lead to mislocation of the source position. The ES is an iterative method that searches for an optimal selection of parameters by probing the global search parameter space (Beyer and Schwefel, 2002; Dirk, 2002). This method uses selection and mutation as natural-resembling operations and it is comparatively faster than gradient-based approaches (Dirk, 2002). Average absorption distributions are then used in the inverse source problem. To find the solution of the inverse source problem, the CW-SP_3 equations are solved by the FDM. A linear relation between model predictions and source density distribution is derived, $\mathbf{P} = \mathbf{A}_{(FDM)}\mathbf{Q}$ where $\mathbf{A}_{(FDM)}$ is an $m \times n$ matrix which appears similarly to $\mathbf{A}_{(FEM)}$, see Eq. (6.106). To speed-up the calculations, the reciprocity principle is used (Dehghani et al., 2008). The inverse source problem posed by the linear system of equations $\mathbf{A}_{(FDM)}\mathbf{Q} = \mathbf{M}$ is solved by the algebraic reconstruction technique (ART) (Natterer, 2001). The ART (or Kaczmarz method) is a method for solving linear systems of equations that exploit sparseness (Natterer, 2001; Nikazad, 2008). Finally, the ART iteratively computes the solution using the following formula

$$Q_{k+1} = Q_k + \xi_k \left(\frac{M_i - \langle a_i, Q_k \rangle}{\|a_i\|^2} \right) a_i\,, \tag{6.107}$$

where $\langle\ ,\ \rangle$ represents the scalar product, ξ_k is a relaxation parameter, $i = k \bmod m + 1$, M_i is the ith component of $\mathbf{M}$ and a_i is the ith row of the matrix $\mathbf{A}_{(FDM)}$.

In (Tian et al., 2010), the CW-SP_3 equations are discretized using the FEM. A linear relation between the exitance values and the source density distribution is derived. The solution to the inverse source problem is determined by minimizing the energy function $E(\mathbf{Q})$

$$E(\mathbf{Q}) = \left\| \mathbf{A}_{(FEM)}\mathbf{Q} - \mathbf{M} \right\| + \lambda \left\| \mathbf{Q} \right\| , \tag{6.108}$$

which is a particular case of the objective function appearing in Eq. (6.106), considering the penalty function as the L_2 norm of $\mathbf{Q}$. To optimize the energy function given in Eq. (6.108), a gradient-free optimization method called generalized graph cuts (GGC) is employed. GGC is an efficient optimization tool that is applied in computer vision and graphics (Boykov and Kolmogorov, 2004; Kolmogorov and Zabih, 2004; Kolmogorov and Rother, 2007). Lately, GGC has been rediscovered in other disciplines including bioluminescence imaging (Tian et al., 2010; Liu et al., 2010). As described in (Tian et al., 2010; Liu et al., 2011), a graph containing the FEM mesh is built and an equivalent graph expression for Eq. (6.108) is found. Then, the energy function Eq. (6.108) is minimized using a quadratic pseudo-boolean optimization method (Kolmogorov and Rother, 2007).

6.6.2 Fluorescence imaging

Fluorescence imaging by direct methods relies on active, or activatable, probes which are excited by external sources or specific enzymes (Rao et al., 2007; Klose, 2009, 2012). Indirect methods are used in gene activation and regulation with the introduction of transgenes, which induce the production of fluorescence proteins (Rao et al., 2007). Fluorescent probes possess their specific properties in terms of converting excitation light into emitted (fluoresced) light. These are the molar extinction coefficient ε and the quantum yield ς. In TD methods, the fluorescence lifetime τ, which characterizes the fluorescence emission dynamics is also included in the studies. The fluorescence lifetime is sensitive to local metabolite concentrations or environmental conditions within tissues (Nothdurft et al., 2009), and thus provides information about such factors. When distributed into biological tissues, fluorescent probes contribute to the overall absorption (absorption of a fluorophore being equal to ε times the concentration C). Fluorescence imaging requires a forward model that maps fluorophore distribution to fluorescence data, as the straightforwardly used DE (Ntziachristos, 2006; Zacharopoulos et al., 2010; Zhu et al., 2011). However, in the presence of high absorption, see for example (Comsa et al., 2008) and references in (Bouza Domínguez and Bérubé-Lauzière, 2011a), the DE cannot compete with quantitativeness of biomarkers offered by nuclear imaging techniques.

With this perspective, fluorescence tomography has been recently attempted with the CW-SP_N model as the forward model for describing both the excitation (ex) and the fluorescence (fl) light propagation (Klose, 2010b; Klose and

Pöschinger, 2011; Klose et al., 2011; Klose, 2012). Thus, the model consists in a system of two SP_N equations as

$$\left[D_r^{(i)} + \mathbf{C}^{(i)}\right] \mathbf{\Phi}^{(i)}(\mathbf{r}) = \mathbf{Q}^{(i)}(\mathbf{r}) \,, \quad i = ex, fl \,, \tag{6.109}$$

where the components of the source vector $\mathbf{Q}^{(fl)}(\mathbf{r})$ are proportional to the fluorescence source term $Q^{fl}(\mathbf{r})$, which quantify the interaction between the excitation light and the fluorescent response

$$Q^{fl}(\mathbf{r}) = \varsigma \varepsilon C \psi_0^{ex}(\mathbf{r}) \,. \tag{6.110}$$

Eq. (6.109) is discretized using the FDM and the resulting algebraic system of equations is solved by the successive over-relaxation (SOR) method (Klose et al., 2011; Saad, 2003). Then, the inverse problem is posed similarly to Eq. (6.106) and iteratively solved for C using an expectation-maximization (EM) method (Dempster et al., 1977; Wernick and Aarsvold, 2004). Based on the abovementioned works, notable improvements have been achieved in the area of hyperspectral excitation-resolved fluorescence tomography. Here, fluorophores with broad molar extinction spectra are used as probes, and allow exploiting the spectral properties of tissue oxy- and deoxy-hemoglobin components in ranges where their molar extinction varies widely (Klose and Pöschinger, 2011). In another work, the authors employ the FEM as the discretization method for Eqs. (6.109) (Han et al., 2010). Also, the usually sparse/spatially-reduced properties of fluorophore distributions are used in a regularization scheme as *a priori* information. The solution of the inverse problem is searched by an iteratively reweighted scheme which approximates the L_1-norm regularization (Han et al., 2010; Wang et al., 2011). A sampling procedure (visual inspection) is chosen to determine the optimal value for the regularization parameter.

In FD, a similar formulation to Eq. (6.109) has been derived (Lu et al., 2010), this time using the FD-SP_N equations and introducing the complex-valued nth-order transport coefficients Eq. (6.81). The resulting equations have been discretized through the FEM and a parallel adaptive FEM is used. Finally, the quest for lifetime imaging has recently triggered the development of new TD forward models based on the TD-pSP_N equations (Bouza Domínguez and Bérubé-Lauzière, 2011a). In this work, a set of TD-pSP_N equations has been obtained for describing the time-dependent propagation of the excitation light and the ensuing fluorescent response. This time, the time-dependent fluorescence source term $Q^{fl}(\mathbf{r}, t)$ quantifies the temporal interaction between the excitation field and the fluorescence emission. The coupling between excitation and fluorescence emission can be described through a convolution operation as

$$Q^{fl}(\mathbf{r}, t) = \frac{\varsigma \varepsilon C(\mathbf{r})}{\tau} \int_{t'=0}^{t'=t} \psi^{ex}(\mathbf{r}, t') \exp\left(\frac{t' - t}{\tau}\right) \mathrm{d}t' \,. \tag{6.111}$$

A FEM/FDM numerical implementation is described in the same work. Numerical simulations with three-dimensional biological media provide new information on the influence of fluorophore distribution on the TD curves, see Fig. 6.8. This approach should lead, in a near future, to the solution of a nonlinear inverse problem for recovering lifetime spatial maps τ.

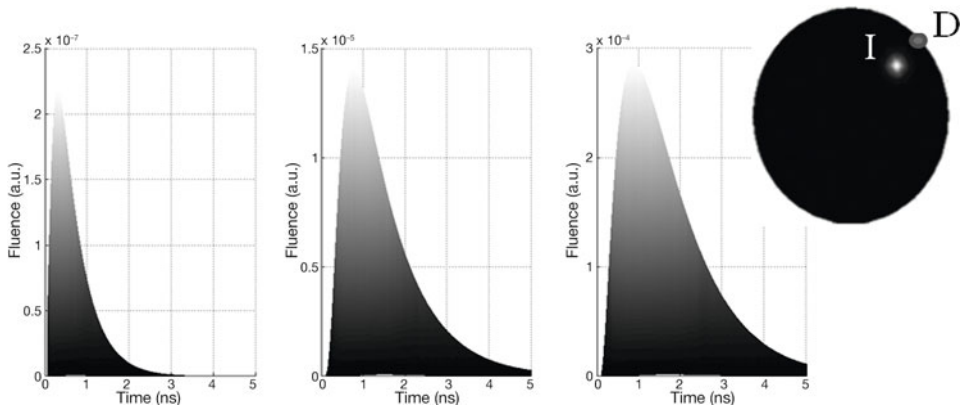

Fig. 6.8. Numerical simulations for a cylindrical homogeneous medium ($\eta = 1.4$, $\mu_a = 0.13\,\mathrm{cm}^{-1}$, $\mu_s = 100\,\mathrm{cm}^{-1}$ and $g = 0.9$.) with an absorptive fluorescent inclusion ($\mu_a = 3\,\mathrm{cm}^{-1}$ and $\tau = 0.56\,\mathrm{ns}$) located at point I; see tomographic cut of the cylinder at right. Plots represent the fluorescence TD curves at point D, the closest point to I. We consider three different fluorophore distributions (left to right): a point inclusion, a small spherical inclusion and a Gaussian distributed inclusion. There is a noteworthy change in the shape of the curve.

6.6.3 Cerenkov luminescence imaging

Cerenkov luminescence imaging (CLI) is an evolving technology that uses optical photons generated by positron emission tomography (PET) radiotracers (Robertson et al., 2009; Liu et al., 2010b; Boschi et al., 2009; Spinelli et al., 2010, Dothager et al., 2010). Cerenkov radiation is created by high-energy charged particles that momentarily exceed the speed of light in the medium in which they propagate (Robertson et al., 2009). PET radionuclides and most of β-emitting radionuclides with biomedical applications produce measurable Cerenkov radiation in water or in tissue (Boschi et al., 2009). The Cerenkov light spectrum is continuous, in contrast to fluorescence or emission spectra that have characteristic spectral peaks. The relative intensity is proportional to frequency thus: higher frequencies (ultraviolet/blue) are most intense. At ultraviolet/blue wavelengths, Cerenkov radiation is highly absorbed by tissue components (water, hemoglobin, cytochromes, etc.). Large absorption coefficients make the DE less accurate and transport calculations are required (Hielscher et al., 1998).

Cerenkov radiation can be detected by current optical imaging methods. Retrieving the distribution of Cerenkov optical sources becomes an inverse luminescence source problem, as in bioluminescence tomography. Moreover, radionuclide activity levels which are necessary to inject and produce detectable optical signals are typical of small animal imaging (Spinelli et al., 2010; Li et al., 2010). Therefore, CLI provides considerable advantages regarding drug discovery and in general, biomedical research. Cerenkov luminescence tomography for small animal imaging has been attempted with success and even a multispectral approach has been developed (Spinelli et al., 2011). However, the reconstruction results are limited by the use of the DE as the forward model (discretized using the FEM) in

media where large absorption occurs in small geometries. In addition, the inverse source problem is posed as an unconstrained optimization problem which accentuates the ill-posedness. Typically, a linear least-squares type, objective function with a Tikhonov regularization term is employed (Spinelli et al., 2011; Zhong et al., 2011). Then, the solution can be iteratively retrieved by the preconditioned conjugate gradient (PCG) method (Li et al., 2010) or a non-negative least square optimization algorithm (Spinelli et al., 2011).

Lately, the FEM-discretized CW-SP_3 equations have been used in a model-based reconstruction algorithm to perform whole-body Cerenkov luminescence tomography (Zhong et al., 2011b). The inverse source problem is posed as a linear least-squares objective function with a regularization term or penalty function similarly as in Eq. (6.106). The penalty function is set as a linear combination of L_2 (ridge-regression penalty) and L_1 (lasso-regression penalty) norms of the source density distribution Q. This type of regularization is known as *elastic net regularization* and is used for moderating both smoothing and sparsity effects in the reconstruction (Friedman et al., 2010; Van der Kooij, 2007). The components of the vector $\mathbf{Q}$ are computed by first applying a soft-threshold operation, to account for lasso penalty, and consequently a proportional shrinkage, to account for the ridge penalty. Details of the algorithm and its derivation can be found in (Friedman et al., 2010). In (Zhong et al., 2011b), a number of experiments concerning small animal imaging are performed. A comparison between DE and SP_3-based reconstructions using the mentioned algorithm is carried out. The impact of the high-absorption tissues ($\sim 1\,\mathrm{cm}^{-1}$) is evaluated. There is a substantial reduction in the source localization error (more than an order of magnitude) when the CW-SP_3 equations serve as the forward model. Thus, the work strongly supports the use of the CW-SP_N model in CLI preclinical studies and opens a pathway to clinics, where the use radioactive contrast agents is widely accepted. More recently, Klose has discussed the use of the SP_3 equations for Cerenkov light tomography in a multi-spectral framework (Klose, 2012).

6.7 Summary

Light propagation models based on the SP_N approximation have been derived, implemented, and used to solve problems in biomedical optics during the last decade. In the literature, both the standard RTE and the source-divergence RTE are employed to obtain low-order transport models by introducing the SP_N approximation. In particular, the equations derived from the source-divergence RTE are able to correctly describe light propagation near point sources, a common physical situation in biomedical optics. Applying the SP_N approximation to the diffuse component of the radiance results in a better description of radiative transport in tissues since angular dependencies are attenuated with the reduced diffuse components formulation. SP_N equations have been obtained for steady state, frequency and time domains. Steady-state and frequency-domain SP_N equations are equivalent under a simple transformation of the transport coefficients into complex coefficients. Time-domain SP_N models have different forms in dependence of the derivation. In particular, the time-domain parabolic SP_N equations constitute the light propagation model that has been most studied thus far for applications in biomedical

optics. SP_N models have been extended to describe luminescent light transfer in biological tissues.

Recently, SP_N models have been employed in DOT and luminescence imaging with significant success. Image reconstructions of absorption and scattering inhomogeneities show an appreciable improvement in localization and quantitativeness in comparison to DE results. Furthermore, the presence of artifacts and cross-talk effects is reduced by the use of SP_N-based DOT algorithms. In inverse source problems (see references cited in Section 6.6), DE-based results have been improved through the use of SP_N-based algorithms. By accurately modeling Cerenkov light propagation in biological tissues, the SP_N equations have also opened a way to satisfactory radionuclide and optical images co-registration. Additionally, SP_N—based CLI offers an alternative (with both functional and anatomical information) to costly PET instrumentation, with no limitations regarding clinically approved targeted agents as in other luminescence imaging modalities. As a further step in CLI, optical signals can be reinforced by spectrally coupling Cerenkov radiation at ultraviolet/blue wavelengths to far-red and near-infrared emitting quantum nanoparticles or fluorophores, resulting in an improvement of reconstructed images (Dothager et al., 2010).

These results demonstrate that the SP_N models are an alternative to computationally costly transport calculations (calculations are speeded-up by near to two orders of magnitude), and a solution to DE failures in a considerable number of experimental situations. In general, the reconstructions algorithms that employ SP_N-based forward models have been evolving by including spectral information and constrained optimization features. Further efforts should be addressed on (*i*) improving the numerical schemes for calculating the model predictions, (*ii*) reducing the ill-posedness of the inverse problem by imposing constraints in both the parameter space (optical coefficients) and the forward model, and (*iii*) augmenting the robustness of the inverse problem formulation, e.g. in the choice of the objective function.

Acknowledgments

J. Bouza-Domínguez acknowledges financial support from the FQRNT (Québec – Programme de bourses d'excellence pour étudiants étrangers – PBEEE). Y. Bérubé-Lauzière acknowledges financial support from an NSERC Discovery Grant (Canada) for the present work. Yves Bérubé-Lauzière is member of the FRQ-S-funded Centre de recherche clinique Étienne-Le Bel.

References

Abramowitz, M., and Stegun I. A., 1965: *Handbook of Mathematical Functions: with Formulas, Graphs, and Mathematical Tables*, Dover Publications: Mineola, U.S.A.

Agarwal, R. P., 2000: *Difference Equations and Inequality: Theory, Methods, and Applications*, CRC Press: New York.

Alexandrakis, G., Rannou, F. R., Chatziioannou, A. F., 2005: Tomographic bioluminescence imaging by use of a combined optical-PET (OPET) system: a computer simulation feasibility study, *Phys. Med. Biol.*, **50**, 4225–4241.

Alexandrakis, G., Rannou, F. R., Chatziioannou, A. F., 2006: Effect of optical property estimation accuracy on tomographic bioluminescence imaging: simulation of a combined optical–PET (OPET) system, *Phys. Med. Biol.*, **51**, 2045–2053.

Arridge, S. R., 1999: Optical tomography in medical imaging, *Inverse Probl.*, **15**, R41–R93.

Arridge, S. R., and Schotland, J. C., 2009: Optical tomography: forward and inverse problems, *Inverse Probl.*, **25**, 123010.

Atalay, M. A., 2006: P_N solutions of radiative heat transfer in a slab with reflective boundaries, *J. Quant. Spectr. Rad. Transfer*, **101**, 100–108.

Benson, S. J., and Moré, J. A. 2001: Limited-memory variable-metric algorithm for bound-constrained minimization, *Technical Report ANL/MCS-P909-0901*, Argonne National Laboratory.

Bérubé-Lauzière, Y., Issa, V., Bouza Dominguez, J., 2009: Simplified spherical harmonics approximation of the time-dependent equation of radiative transfer for the forward problem in time-domain diffuse optical tomography, *Proc. of SPIE*, **7174**, 717403-11.

Beyer, H. G. and Schwefel, H.-P., 2002: Evolution strategies, *Nat. Comput.*, **1**, 3–52.

Boschi, F., Spinelli, A. E., D'Ambrosio, D., Calderan, L., Marengo, M., Sbarbati, A., 2009: Combined optical and single photon emission imaging: preliminary results, *Phys. Med. Biol.*, **54**, L57–L62.

Bouza Domínguez, J., and Bérubé-Lauzière, Y., 2010: Diffuse light propagation in biological media by a time-domain parabolic simplified spherical harmonics approximation with ray-divergence effects, *Appl. Opt.*, **49**, 1414–1429.

Bouza Domínguez, J., and Bérubé-Lauzière, Y., 2011a: Light propagation from fluorescent probes in biological tissues by coupled time-dependent parabolic simplified spherical harmonics equations, *Biomed. Opt. Express*, **2**, 817–837.

Bouza Domínguez, J., and Bérubé-Lauzière, Y., 2011b: Diffuse optical tomography of absorption in biological media using time-dependent parabolic simplified spherical harmonics equations, *Proc. SPIE*, **8088**, 80880S.

Bouza Domínguez, J., and Y. Bérubé-Lauzière Y., 2012: Diffuse optical tomographic imaging of biological media by time-dependent parabolic SPN equations: a two-dimensional study. *J. Biomed. Optics*, 17(8):086012-1-086012-14.

Born, M., and Wolf, E., 2003: Principles of Optics, 7th edn, Cambridge University Press: Cambridge, UK.

Boykov, Y., and Kolmogorov, V., 2004: An experimental comparison of min-cut/max-flow algorithms for energy minimization in vision, *IEEE Trans. Patt. Anal. and Mach. Intell.*, **26**, 1124–1137.

Brantley, P. S., and Larsen, E. W., 2000: The simplified P3 approximation, *Nucl. Sci. Eng.*, **134**, 1–21.

Burgess, S. A., Ratner, D., Chen, B. R., Hillman, E. M. C., 2010: Fiber-optic and articulating arm implementations of laminar optical tomography for clinical applications, *Biomed. Opt. Express*, **1**, 780–790.

Case, K. M., and Zweifel, P. F., 1967: Linear Transport Theory, Addison-Wesley.

Chandrasekhar, S., 1960: Radiative Transfer, Dover Publications: New York.

Chen, B., Stamnes, K., Stamnes, J. J., 2001: Validity of the Diffusion Approximation in Bio-Optical Imaging, *Appl. Opt.*, **40**, 6356–6366.

Chu, M., Vishwanath, K., Klose, A. D., Dehghani, H., 2009: Light transport in biological tissue using three-dimensional frequency-domain simplified spherical harmonics equations, *Phys. Med. Biol.*, **54**, 2493–2500.

Chu, M., and Dehghani, H., 2009: Image reconstruction in diffuse optical tomography based on simplified spherical harmonics approximation, *Opt. Express*, **16**, 17780–17791.

Contag, C. H., and Bachmann, M. H., 2002: Advances in In Vivo bioluminescence imaging of gene expression. *Annu. Rev. Biomed. Eng.*, **4**, 235–260.

Comsa, D. C., Farrell, T. J., Patterson, M. S., 2008: Quantitative fluorescence imaging of point-like sources in small animals, *Phys. Med. Biol.*, **53**, 5797–5814.

Davidson, B., and Sykes, J. B., 1957: Neutron Transport Theory, Oxford University Press: Oxford.

Davis, T. A., 2006: Direct Methods for Sparse Linear Systems (Fundamentals of Algorithms), SIAM: Philadelphia.

Dehghani, H., Davis, S. C., Pogue, B. W., 2008: Spectrally resolved bioluminescence tomography using the reciprocity approach, *Med. Phys.*, **35**, 4863–4871.

Dehghani, H., Eames, M. E., Yalavarthy, P. K., Davis, S. C., Srinivasan, S., Carpenter, C. M., Pogue, B. W., Paulsen, K. D., 2009a: Near infrared optical tomography using NIRFAST: Algorithm for numerical model and image reconstruction, *Commun. Numer. Meth. Eng.*, **25**, 711–732.

Dehghani, H., Srinivasan, S., Pogue, B. W., Gibson, A., 2009b: Numerical modelling and image reconstruction in diffuse optical tomography, *Phil. Trans. Royal. Soc. A*, **367**, 3073–3093.

Dempster, A. P., Laird, N. M., Rubin, D. B., 1977: Maximum likelihood from incomplete data via the EM algorithm, *J. R. Stat. Soc. Ser. B Stat. Methodol.*, **39**, 1–38.

de Oliveira, C. R. E., 1986: An arbitrary geometry finite element method for multigroup neutron transport with anisotropic scattering, *Prog. Nucl. Energ.*, **18**, 227–236.

Dirk, V. A., 2002: *Noisy Optimization with Evolution Strategies (Genetic Algorithms and Evolutionary Computation)*, Springer: New York.

Dothager, R. S., Goiffon, R., Jackson, E., Harpstrite, S., Piwnica-Worms, D., 2010: Cerenkov radiation energy transfer (CRET) imaging: a novel method for optical imaging of PET isotopes in biological systems, PLoS ONE, 5, e13300.

Ducross, N., 2009: *Tomographie optique de fluorescence dans les milieux diffusants: apport de l'information temporelle*, Ph.D. thesis, Université Claude Bernard – Lyon I.

Duderstadt, J. J., and Martin, W. R., 1979: *Transport Theory*, John Wiley and Sons: New York.

Elwell, C. E., and Cooper, C. E., 2011: Making light work: illuminating the future of biomedical optics, *Phil. Trans. Royal Soc. A*, **369**, 4358–4379.

Faris, G. W., 2002: Diffusion equation boundary conditions for the interface between turbid media: a comment, *J. Opt. Soc. Am. A*, **19**, 519–520.

Fletcher, J., 1983: Solution of the multigroup neutron transport equation using spherical harmonics, *Nucl. Sci. Eng.*, **84**, 33–46.

Frank, M., Klar, A., Larsen, E., Yasuda, S., 2007: Time-dependent simplified P_N approximation to the equations of radiative transfer, *J. Comput. Phys.*, **226**, 2289–305.

Friedman, J. H., Hastie, T., Tibshirani, R., 2010: Regularization paths for generalized linear models via coordinate descent, *J. Stat. Softw.*, **33**, 1–22.

Gelbard, E. M., 1960: Application of spherical harmonics methods to reactor problems, WAPD-BT-20, Bettis Atomic Power Laboratory.

Gockenbach, M. S., 2006: *Understanding and Implementing the Finite Element Method*, SIAM: Philadelphia.

Han, D., Tian, J, Liu, K., Feng, J., Zhang, B., Ma, X., Qin, C., 2010: Sparsity-promoting tomographic fluorescence imaging with simplified spherical harmonics approximation, *IEEE Trans. Biomed. Eng.*, **57**, 2564–2567.

Hazra, S. B., 2010: PDE-constrained optimization methods, in *Large-Scale PDE-Constrained Optimization in Applications*, Springer-Verlag: New York.

Hielscher, A. H., Alcouffe, R. E., Barbour, R. L., 1998: Comparison of finite-difference transport and diffusion calculations for photon migration in homogeneous and heterogeneous tissues, *Phys. Med. Biol.*, **43**, 1285–1302.

Hielscher, A. H., 2005: Optical tomography imaging of small animals, *Curr. Opin. Biotechnol.*, **16**, 79–88.

Hielscher, A. H., Kim, H. K., Klose, A. D., 2011: Forward models of light transport in biological tissue, in *Handbook of Biomedical Optics*, CRC Press: Boca Raton.

Howell, J. R., Siegel, R., Menguc, M. P., 2010, *Thermal Radiation Heat Transfer*, 5th edn, CRC Press: New York.

Ishimaru, A., 1978: *Wave Propagation and Scattering in Random Media*, Academic Press: New York.

Jin, J., 2002: *The Finite Element Method in Electromagnetics*, John Wiley and Sons Inc.: New York.

Klose, A. D., and Larsen, E., 2006: Light transport in biological tissue based on the simplified spherical harmonics equations, *J. Comput. Phys.*, **220**, 441–70.

Klose, A. D., and Hielscher, A. H., 2008: Optical tomography with the equation of radiative transfer, *Int. J. Numer. Method Heat Fluid Flow.*, **18**, 443–464.

Klose, A. D., 2009: Radiative transfer of luminescence light in biological tissue, in *Light Scattering Reviews 4*, A. A. Kokhanovsky, ed., Springer – Praxis: Chichester, pp. 293–345.

Klose, A. D., Beattie, B. J., Dehghani, H., Vider, L., Le, C., Ponomarev, V., Blasberg, R., 2010: In vivo bioluminescence tomography with a blocking-off finite-difference SP_3 method and MRI/CT co-registration, *Med. Phys.*, **37**, 329–338.

Klose, A. D., 2010a: The forward and inverse problem in tissue optics based on the radiative transfer equation: A brief review, *J. Quant. Spectrosc. Radiat. Transfer*, **111**, 1852–1853.

Klose, A. D., 2010b: Hyperspectral excitation-resolved fluorescence tomography with the SP_3 equations, Proc. OSA-BIOMED Conf., BSuD51.

Klose A. D., and Pöschinger, T., 2011: Excitation-resolved fluorescence tomography with simplified spherical harmonics equations, *Phys. Med. Biol.*, **56**, 1443–1469.

Klose, A. D., Tekabe, Y., Johnson, L., 2011: Hyperspectral fluorescence tomography Of quantum dots using the simplified spherical harmonics equations, *Proc. SPIE*, 8088, 80880V.

Klose, A. D., 2012: Multispectral optical luminescence tomography with the simplified spherical harmonics equations, in *Light Scattering Reviews 7*, A. A. Kokhanovsky, ed., Springer – Praxis, Chichester, UK.

Kolmogorov, V., and Zabih, R., 2004: What energy functions can be minimized via graph cuts?, *IEEE Trans. Patt. Anal. and Mach. Intell.*, **26**, 147–159.

Kolmogorov, V., and Rother, C., 2007: Minimizing non-submodular functions with graph cuts-a review, *IEEE Trans. Patt. Anal. and Mach. Intell.*, **29**, 1274–1279.

Kotiluoto, P., Pyyry, J., Helminen, H., 2007: Multitrans SP_3 code in coupled photon-electron transport problems, *Radiat. Phys. Chem.*, **76**, 9–14.

Larusson, F., Fantini, S., Miller, E. L., 2011: Hyperspectral image reconstruction for diffuse optical tomography, *Biomed. Opt. Express*, **2**, 946–965.

Larsen, E. W., Morel, J. E., McGhee, J. M., 1996: Asymptotic derivation of the multigroup P_1 and simplified P_N equations with anisotropic scattering, *Nucl. Sci. Eng.*, **123**, 328.

Larsen, E. W., Thömmes, G., Klar, A., Seaïd, M., Götz T., 2002: Simplified P_N approximations to the equations of radiative heat transfer and applications, *J. Comp. Phys.*, **183**, 652–675.

Lay, D. C., 2011: *Linear Algebra and Its Applications*, 4th edn, Addison-Wesley, Boston.

Li, C., Mitchell, G., Cherry, S., 2010: Cerenkov luminescence tomography for small-animal imaging, Opt. Lett., **35**, 1109–1111.

Liemert, A., and Kienle, A., 2010: Analytical solutions of the simplified spherical harmonics equations, *Opt. Lett.*, **35**, 3507–3509.

Liemert, A., and Kienle, A., 2011a: Comparison between radiative transfer theory and the simplified spherical harmonics approximation for a semi-infinite geometry, *Opt. Lett.*, **36**, 4041–4043.

Liemert, A., and Kienle, A., 2011b: Analytical solution of the radiative transfer equation for infinite-space fluence, *Phys. Rev. A*, **83**, 039903.

Liu, K., Tian, J., Lu, Y-J., Qin, C-H., Zhu, S-P., Zhang, X., 2010: A fast bioluminescent source localization method based on generalized graph cuts with mouse model validations, *Opt. Express*, **18**, 3732–3745.

Liu, H., Ren, G., Miao, Z., Zhang, X., Tang, X., Han, P., Ghambir, S. S. Cheng Z., 2010b: Molecular optical imaging with radioactive probes, *PLoS ONE*, **5**, e9470.

Liu, K. Tian, J., Sr., Qin, C., Yang, X., Zhu, S., Han, D., Ping Wu, Xiaoqian Dai, 2011: In vivo heterogeneous tomographic bioluminescence imaging via a higher-order approximation forward model, *Proc. SPIE*, **7965**, 79650C.

Lu, Y., Douraghy, A., Machado, H. B., Stout, D., Jie, T., Herschman, H., Chatziioannou, A. F., 2009: Spectrally resolved bioluminescence tomography with the third-order simplified spherical harmonics approximation, *Phys. Med. Biol.*, **54**, 6477–6493.

Lu, Y., Zuh, B., Shen, H., Rasmussen, J. C., Wang G., Sevick-Muraca, E. M., 2010: A parallel adaptive finite element simplified spherical harmonics approximation solver for frequency domain fluorescence molecular imaging, *Phys. Med. Biol.*, **55**, 4625-4645.

Martí López, L., Bouza Domínguez, J., Hebden, J. C., Arridge, S. R., Martínez Celorio, R. A., 2003: Validity conditions for the radiative transfer equation, *J. Opt. Soc. Am. A*, **20**, 2046–2056.

Marshak, R. E., 1947: Note on the spherical harmonic method as applied to the Milne problem for a sphere, *Phys. Rev.*, **71**, 443–446.

Melnikova, I., Kuznetsov, A., Seroukhova, O., Pozdnyakov, D., Vasilyev, A., 2012: Remote Sensing of the Environment and Radiation Transfer. An Introductory Survey, Springer Verlag, New York.

Mitchell, G. S., Gill, R. K., Boucher, D. L., Li C., Cherry, S. R., 2011: In vivo Cerenkov luminescence imaging: a new tool for molecular imaging, *Phil. Trans. Royal Soc. A*, **28**, 369, 4605–4619.

Modest, M. F., 2003, *Radiative Heat Transfer*, 2nd edn, Academic Press, New York.

Montejo, L. D., Klose, A. D., Hielscher, A. H., 2010: Implementation of the equation of radiative transfer on block-structured grids for modeling light propagation in tissue, *Biomed. Opt. Express*, **1**, 861-878.

Montejo, L. D., Kim, H. K., Hielscher, A. H., 2011: A finite volume algorithm for modeling light transport with the time-independent simplified spherical harmonics approximation to the equation of radiative transfer, *Proc. SPIE*, **7896**, 78960J.

Naser, M. A., and Patterson, M. S., 2011: Improved bioluminescence and fluorescence reconstruction algorithms using diffuse optical tomography, normalized data, and optimized selection of the permissible source region, *Biomed. Opt. Express*, **2**, 169–184.

Natterer, F., 2001: *The Mathematics of Computerized Tomography*, SIAM, Philadephia.

Nikazad, T., 2008: *Algebraic reconstruction methods*, Ph.D. thesis, Linköping University.

Nocedal, J., and Wright, S., 2006: Sequential Quadratic Programming, in *Numerical Optimization*, Springer Verlag, New York.

Nothdurft, R. E., Patwardhan, S. V., Akers, W., Yunpeng, Y., Achilefu, S., Culver, J. P., 2009: In vivo fluorescence lifetime tomography, *J. Biomed. Opt.*, **14**, 024004.

Ntziachristos, V., 2006: Fluorescence molecular imaging, *Annu. Rev. Biomed. Eng.*, **8**, 1–33.

Pleijhuis, R. G. Langhout, G. C., Helfrich, W., Themelis, G., Sarantopoulos, A.,, Crane, L. M., Harlaar, N. J., de Jong, J. S., Ntziachristos, V., van Dam, G. M., 2011: Near-infrared fluorescence (NIRF) imaging in breast-conserving surgery: assessing intra-operative techniques in tissue-simulating breast phantoms, *Eur. J. Surg. Oncol.*, **37**, 32–39.

Press, W. H., Teukolsky, S. A., Vetterling, W. T., Flannery, B. P., 2007: Numerical Recipes 3rd Edition: The Art of Scientific Computing, Cambridge University Press, Cambridge, UK.

Rao, J., Dragulescu-Andrasi, A., Yao, H., 2007: Fluorescence imaging in vivo: recent advances, *Curr. Opin. Biotechnol.*, **18**, 17–25.

Ripoll, J., 2000: Light diffusion in turbid media with biomedical application, Ph.D. thesis, Universidad Autónoma de Madrid.

Robertson, R., Germanos, M. S., Li, C., Mitchel, G. S., Cherry, S. R., Silva, M. D., 2009: Optical imaging of Cerenkov light generation from positron-emitting radiotracers, *Phys. Med. Biol.*, **54**, N355–365.

Saad, Y., 2003: Iterative Methods for Sparse Linear Systems, SIAM, Philadelphia.

Spinelli, A. E., D'Ambrosio, D., Calderan, L., Marengo, M., Sbarbati, A., Boschi, F., 2010: Cerenkov radiation allows in vivo optical imaging of positron emitting radiotracers, *Phys. Med. Biol.*, **55**, 483–495.

Spinelli, A. E., Kuo, C., Rice, B. W., Calandrino, R., Marzola, P., Sbarbati, A., Boschi, F., 2011: Multispectral Cerenkov luminescence tomography for small animal optical imaging, *Opt. Express*, **19**, 12605–12618.

Strang, G., 2005: *Linear Algebra and its Applications*, 4th edn, Brooks Cole, Stamford.

Talukdar, P., 2006: Discrete transfer method with the concept of blocked-off region for irregular geometries, *J. Quant. Spectr. Rad. Transfer*, **98**, 238–248.

Tarvainen, T., 2006: *Computational methods for light transport in optical tomography*, Ph.D. thesis, University of Kuopio.

Tian, J., Liu, K., Lu, Y., Qin, C., Yang, X., Zhu, S., Han, D., Feng, J., Ma, X., Chang, Z., 2010: Evaluation of the simplified spherical harmonics approximation in bioluminescence tomography through heterogeneous mouse models, *Opt. Express*, **18**, 20988–21002.

Tomasevic, D. I., and Larsen, E. W., 1996: The simplified P2 approximation, *Nucl. Sci. Eng.*, **122**, 309–325.

Van der Kooij, A., 2007: *Prediction accuracy and stability of regression with optimal scaling transformations*, Ph.D. thesis, University of Leiden.

Van Rossum, M. C. W., and Nieuwenhuizen, Th. M., 1999: Multiple scattering of classical waves: microscopy, mesoscopy, and diffusion, *Rev. Mod. Phys.*, **71**, 313–371.

Versteeg, H., and Malalasekera, W., 2007: An Introduction to Computational Fluid Dynamics: The Finite Volume Method, Prentice Hall: New Jersey.

Vo-Dinh T. (ed.), 2003: Biomedical Photonics Handbook, CRC Press: Boca Raton.

Wang, L., and Wu, H., 2007, Biomedical Optics: Principles and Imaging, Wiley-Interscience, Hoboken, NJ.

Wang, J., Davis, S. C., Srinivasan, S., Jiang, S., Pogue, B. W., Paulsen, K. D., 2008: Spectral tomography with diffuse near-infrared light: inclusion of broadband frequency domain spectral data, *J. Biomed. Opt.*, **13**, 041305-041305.

Wang, Y., Yagola, A. G., Yang, C., 2011: Optimization and Regularization for Computational Inverse Problems and Applications, Springer Verlag: New York.

Website of Toolkit for Advanced Optimization (TAO). Consulted January, 10th, 2012. http://www.mcs.anl.gov/research/projects/tao/.

Weissleder, R., and Ntziachristos, V., 2003: Shedding light onto live molecular targets, *Nat. Med.*, **9**, 123–128.

Welsh, D. K., and Kay S. A., 2005: Bioluminescence imaging in living organisms, *Curr. Opin. Biotechnol.*, **16**, 73–78.

Wernick, M. N., and Aarsvold, J. N., 2004: Emission Tomography: The Fundamentals of PET and SPECT, Academic Press: San Diego.

Willmann, J. K., van Bruggen, N., Dinkelborg, L. M., Gambhir, S. S., 2008: Molecular imaging in drug development, *Nat. Rev. Drug Discov.*, **7**, 591–607.

Wright, S., Schweiger, M., Arridge, S. R., 2007: Reconstruction in optical tomography using the P_N approximations, *Meas. Sci. Technol.*, **18**, 79–86.

Xu, G., Piao, D., Bunting, C. F., Dehghani, H., 2010: The pain and gain of DC-based diffuse optical tomography reconstruction – New insights into an old-like problem, OSA-BIOMED Conf., BSuD54.

Xu, G., Piao, D., Dehghani, H., 2011: The utility of direct-current as compared to frequency domain measurements in spectrally-constrained diffuse optical tomography toward cancer imaging technology, *Tech. Cancer Res. Treat.*, **10**, 403–416.

Zacharopoulos, A., Garofalakis, A., Ripoll, J., Arridge, S. R., 2010: Development of i nvivo fluorescence imaging with the matrix-free method, *J. Phys.*, **255**, 012006.

Zhong, J., Tian, J., Yang, X., Qin, C., 2011: Whole-body Cerenkov luminescence tomography with the finite element SP_3 method, *Annals of Biomed. Eng.*, **39**, 1728–1735.

Zhong, J., Qin, C., Yang, X., Zhu, S., Zhang, X., Tian, J., 2011b: Cerenkov luminescence tomography for in vivo radiopharmaceutical imaging, *Int. J. Biom. Imag.*, 641618.

Zhu, Q., Dehghani, H., Leblond, F., El-Ghussein, F., Pogue, B. W., 2011: Development and evaluation of a time-resolved near-infrared fluorescence finite element model, *Proc. SPIE*, **7896**, 78960T.

Zhu, Q., Dehghani, H., Tichauer, K. M., Holt, R. W., Vishwanath, K., Leblond, F., Pogue, B. W., 2011: A three-dimensional finite element model and image reconstruction algorithm for time-domain fluorescence imaging in highly scattering media, *Phys. Med. Biol.*, **56**, 7419.